



Extraordinary d–d hybridization in $\text{Co}(\text{Cu})_{0.5}\text{O}_x\text{H}_y$ microcubes facilitates $\text{PhCH}_2\text{O}^*-\text{Co}(\text{IV})$ coupling for benzyl alcohol electrooxidation

Lei Huang^a, Xiongchao Lin^{a,*}, Ke Zhang^a, Jun Zhang^a, Caihong Wang^a, Sijian Qu^b,
Yonggang Wang^a

^a School of Chemical & Environmental Engineering, China University of Mining and Technology (Beijing), D11 Xueyuan Road, Haidian, Beijing 100083, PR China

^b Beijing Research Institute of Coal Chemistry, China Coal Research Institute, Chaoyang, Beijing 100013, PR China

ARTICLE INFO

Keywords:

Benzyl alcohol electrooxidation reaction
Co-based catalysts
Active sites
Synergistic effect
Proton-coupled electron transfer

ABSTRACT

A series of bimetallic hydroxides $\text{Co}(\text{M})_{0.5}\text{O}_x\text{H}_y$ ($\text{M} = \text{Cu}, \text{Ni}, \text{Mn}, \text{Zn}$) were fabricated for the benzyl alcohol oxidation reaction (BAOR). The active origin and synergistic effect of bimetallic electrocatalysts were adequately deciphered. The reaction was found to be principally initiated from the sequential oxidation of Co^{2+} (i.e., Co^{2+} to Co^{3+} to Co^{4+}), followed by the spontaneous proton-coupled electron transfer (PCET) process between Co^{4+} and benzyl alcohol (BA) molecules. Besides, the adsorption free energy of BA molecules on $\text{Co}(\text{Cu})_{0.5}\text{O}_x\text{H}_y$ was successfully optimized by Cu doping owing to the extraordinary d–d orbital hybridization between Co and Cu atom. As a result, an extra high conversion rate (95.3%) of BA and selectivity (98.2%) of benzoic acid were achieved under 0.5 V vs. Hg/HgO . These insights are essential for a comprehensive understanding of the BAOR mechanism and the design of Co-based catalysts.

1. Introduction

Selective oxidation of benzyl alcohol to benzoic acid or benzaldehyde plays a pivotal role in chemical industry, because of their wide utilization in food additives, dye and pharmaceutical intermediates [1–4]. However, the conventional thermocatalytic route has the limitation of low yield, high energy consumption and heavy pollution [5–8]. Electrocatalytic oxidation of benzyl alcohol, using water as the oxygen source and clean electrons as the redox agents, meets the requirement of green chemistry [4]. Designing efficient and cheaper electrocatalysts is of paramount importance for practical application of BAOR.

The active component has considerable impact on the performance of electrocatalysts. Co-based materials possessing fantastic redox reversibility have attracted great interest in electrooxidation reactions (EORs) [9]. In order to promote the catalytic activity, a series of modification approaches, such as vacancy design, heterojunction construction, element doping, and component regulation were performed [10–14]. However, some of these strategies still have their own limitation for facilitating the performance of catalysts. This is attributed to the fact that the EORs is a complex multi-electron transfer process accompanied by valence state change of catalyst components, resulting in the neglect of the real active sites [15,16]. Therefore, the insights into the

origins of catalytic activity are necessary to unveil the EORs mechanism and design efficient Co-based electrocatalysts. At present, the perspective on active site of Co-based catalysts in BAOR or oxygen evolution reaction (OER) remains divergent. Some researchers have proposed the active origin of both BAOR and OER was $\text{CoO}(\text{OH})_{\text{ads}}$ intermediates, which is generated from the electrooxidation of Co^{2+} ions ($\text{Co}^{2+} + 3\text{OH}^- = \text{CoO}(\text{OH})_{\text{ads}} + \text{H}_2\text{O} + \text{e}^-$) [1,11,17,18]. Hence, the conception to promote the catalytic activity by reducing the oxidation potential of Co^{2+} to Co^{3+} is proposed. However, Co^{4+} species were also observed in recent study during water oxidation and supercapacitor using in-situ spectroscopy [9,19–22]. The Co^{4+} ions are considered to be vital intermediates in O–O bond formation and determine the OER activity [19, 20]. Consequently, by adjusting the distribution of Co^{4+} is thought to be able to overcome the sluggish OER kinetics. This perspective is rarely reported in the BAOR. Nevertheless, the applied potential of the BAOR reported in the literature is exceeded the oxidation potential of Co^{3+} to Co^{4+} (0.77 V vs. Ag/AgCl) [19]. Summarily, it is essential to identify the real active site of Co-based catalysts in the BAOR process, which has significance effect on the design and modification of Co-based catalysts and conduce to comprehensively elaborating on the BAOR mechanism.

Optimizing the adsorption free energy of reactant is another feasible approach to promote the catalytic activity. The adsorption free energy is

* Corresponding author.

E-mail address: linxiongchao@163.com (X. Lin).

<https://doi.org/10.1016/j.apcatb.2024.123739>

Received 26 September 2023; Received in revised form 19 December 2023; Accepted 13 January 2024

Available online 15 January 2024

0926-3373/© 2024 Elsevier B.V. All rights reserved.

closely related to the electronic structure of active site. Element doping and defect construction are efficient strategies to regulate the electronic structure [23–25]. The bimetallic hydroxides have attracted widespread attentions, ascribing to their multiple active sites and synergistic effects [14,26]. The rational regulation of the composition and proportion of the bimetallic hydroxides is able to influence the adsorption/desorption ability for crucial reaction intermediates and finally improve the catalytic activity [27]. However, the mechanism of bimetal regulating adsorption energy is still ambiguous.

The main purpose of this work is to identify the real active site of bimetallic hydroxide catalysts and reveal the synergistic effect between bimetals. A series of bimetallic hydroxide catalysts $\text{Co(M)}_{0.5}\text{O}_x\text{H}_y$ ($\text{M} = \text{Cu, Ni, Mn, Zn}$) for BAOR were fabricated by a facile alkali etching method. The electrochemical properties and catalytic performance of these catalysts were evaluated in the 3-electrode system. The active sites of catalysts in the process of BAOR were identified by in-situ Raman spectroscopy and ex-situ XPS spectroscopy. The progressive oxidation of $\text{Co(Cu)}_{0.5}\text{O}_x\text{H}_y$ to $\text{Co(Cu)}_{0.5}\text{O}_2$ was investigated. The PCET process between BA molecules and Co^{4+} species was proposed based on the periodic electrochemical measurements. Moreover, the synergistic effect between Cu and Co atoms was further clarified by theoretical calculation. Eventually, the reaction parameters were further optimized. This work specified the BAOR mechanism and is expected to shed light on the design of Co-based catalysts.

2. Experimental section

2.1. Chemical reagents

Cupric acetate ($\text{Cu}(\text{CH}_3\text{COO})_2$), cobalt nitrate hexahydrate ($\text{Co}(\text{NO}_3)_2 \cdot 6 \text{H}_2\text{O}$), hydrochloric acid (HCl), trisodium citrate dihydrate ($\text{C}_6\text{H}_5\text{Na}_3\text{O}_7 \cdot 2 \text{H}_2\text{O}$), potassium hexacyanocobaltate ($\text{K}_3[\text{Co}(\text{CN})_6]$), and potassium hydroxide (KOH) were purchased from Mreda Co., Ltd. Manganes acetate tetrahydrate ($\text{Mn}(\text{CH}_3\text{COO})_3 \cdot 4 \text{H}_2\text{O}$), nickel acetate tetrahydrate ($\text{Ni}(\text{CH}_3\text{COO})_2 \cdot 4 \text{H}_2\text{O}$), zinc acetate dihydrate ($\text{Zn}(\text{CH}_3\text{COO})_2 \cdot 2 \text{H}_2\text{O}$), benzyl alcohol, benzaldehyde, benzoic acid, N, N-dimethylformamide (DMF) and ethyl acetate were purchased from Macklin Co., Ltd. All reagents were AR grade. Ni foam (NF) was purchased from Suzhou Sinero technology Co., Ltd.

2.2. Preparation of CoO_xH_y and $\text{Co(M)}_{0.5}\text{O}_x\text{H}_y$ ($\text{M} = \text{Cu, Ni, Mn, Zn}$) microcubes

The synthetic process of Prussian blue analogues (PBAs) was described in Supporting Information. The bimetallic hydroxides CoO_xH_y and $\text{Co(M)}_{0.5}\text{O}_x\text{H}_y$ ($\text{M} = \text{Cu, Ni, Mn, Zn}$) were obtained by alkali etching of PBAs [28]. Primarily, 0.20 g Co-PBAs was dispersed in 10.0 mL anhydrous alcohol by sonication. Then, 17.0 mL of 0.10 M KOH aqueous was poured into the above Co-PBAs suspension. The mixture was oscillated for 5 min and separated by centrifugation. The yellow-green precipitate was eluted with deionized water and anhydrous alcohol until the pH value of the supernatant was neutral. Finally, the powder was dried in vacuum oven at 40 °C for 12 h. Likewise, the $\text{Co(M)}_{0.5}\text{O}_x\text{H}_y$ ($\text{M} = \text{Cu, Ni, Mn, Zn}$) catalysts were synthesized in the same process.

2.3. Preparation of $\text{Co(Cu)}_n\text{O}_x\text{H}_y$ with different copper contents

The synthesis process was performed as the above, and the addition of copper acetate was changed to 0.20 mmol, 0.60 mmol, 1.00 mmol, 1.20 mmol, 1.40 mmol, and 1.80 mmol, respectively. The product was denoted as $\text{Co(Cu)}_n\text{O}_x\text{H}_y$ ($n = 0.1, 0.3, 0.5, 0.6, 0.7, 0.9$).

2.4. Characterization

Scanning electron microscope (SEM, Zeiss Gemini 300, Germany) and transmission electron microscope (TEM, JEOL JEM 2100 F, Japan)

were used to observe the microstructure and crystal surface details of catalyst. The roughness of sample was measured on atomic force microscope (AFM, Bruker Dimension ICON). The composition and crystallinity of the electrocatalysts were analyzed by X-ray diffraction (XRD, Ultima IV, Japan) with Cu K α radiation (36 kV, 30 mA). The scan range was 10° to 70° with a rate of 2° min⁻¹. Fourier transform infrared spectroscopy (FTIR, Bruker Vertex 70, Germany) was used to identify the characteristic peaks of electrocatalyst in the range of 400–4000 cm⁻¹. Raman spectroscopy was carried out on Horiba LabRAM HR Evolution (Japan) using 532 nm laser to determine the molecular structure. The chemical states of electrocatalyst were analyzed by X-ray photoelectron spectroscopy (XPS, Thermo scientific K-Alpha, USA). All XPS characteristic peaks were calibrated by C 1 s (284.8 eV). The elemental quantification was conducted by ICP-OES (Agilent 5110, USA).

In-situ Raman spectra were measured on Horiba LabRAM HR Evolution Raman system (Japan) using 785 nm laser. After catalyst activation, Raman signals at different electrolysis potentials were collected for three times with an interval of 60 s. The electrolytic potential range was 0.1 – 0.6 V vs. Hg/HgO with an interval of 0.10 V. The electrolyte of OER was 1.0 M KOH and that of BAOR was 1.0 M KOH with 10.0 mM BA.

2.5. Electrochemical measurements

The electrochemical properties were evaluated on the CHI 660E electrochemical workstation (CH Instrument Co., Ltd. Shanghai) using a three-electrode technique. The reference electrode and counter electrode were Pt sheet electrode (1 × 1 cm) and Hg/HgO electrode, respectively. The NF (1 × 2 cm) and glass carbon electrode (GCE, 3 mm in diameter) modified with catalysts were used as working electrode. For preparation of the working electrode, the powder catalyst (4.0 mg) was dispersed in 245.0 μL deionized water and 245.0 μL DMF by ultrasonication for 30 min. Then, 10.0 μL Nafion (5 wt%) was dripped into the suspensions. The slurry was undergone an ultrasonic treatment for 60 min. The prepared catalyst ink was dripped on the polished GCE and dried at room temperature with the mass loading of 1.14 mg·cm⁻². The electrocatalyst coating process on the NF was same as that on GCE. The only difference was the mass loading of catalyst (2 mg·cm⁻²).

The electrooxidation process was performed in the H-type electrolytic cell, and the anode and cathode were separated by Nafion 117 membrane. The electrolyte was 1.0 M KOH aqueous solution without or with different concentrations of benzyl alcohol (i.e., 10.0, 20.0, 40.0, 60.0, 80.0, 100.0 mM). Before the test, the electrolyte was saturated with high purity Ar. The working electrode was activated by cyclic voltammetry (CV) between -0.1 and 0.5 V vs. Hg/HgO at 10 mV·s⁻¹ until the stable state were acquired. All the potentials mentioned in this research were converted into reversible hydrogen electrode (RHE) unless otherwise specified: $E_{(\text{RHE})} = E_{(\text{Hg}/\text{HgO})} + 0.925 \text{ V}$. For OER tests, the polarization curves were obtained from the linear sweep voltammograms (LSVs) at a scan rate of 5 mV·s⁻¹. All polarization curves were without adjustment by iR-compensation. The double layer capacitance (C_{dl}) was calculated by CV curves acquired at various scan rates in the potential between 0.32–0.37 V vs. Hg/HgO. The electrochemical impedance spectroscopy (EIS) and phase-Bode plots were conducted under different potentials in the frequency range of 10⁵ Hz to 10⁻² Hz with 0.005 V AC amplitude. For BAOR tests, all measurement conditions were same as the OER, except that the electrolyte needed to be well stirred before each test and the Ar (15 mL·min⁻¹) was maintained aerated during catalytic reaction. The durability of electrocatalysts was evaluated by amperometric i-t curves.

2.6. DFT calculations

The DFT calculations were carried out using the Vienna Ab-initio Simulation Package (VASP) [29] with the frozen-core all-electron projector-augment-wave (PAW) method [30]. The

Perdew-Burke-Ernzerhof (PBE) [31] of generalized gradient approximation (GGA) was adopted to describe the exchange and correlation potential. The cutoff energy for the plane-wave basis set was set to 450 eV. A mono-layer 4×4 Co(OH)₂ slab was used, and the top layer of H atoms were deleted to build CoOOH slab. Four Co atoms were substituted with Cu atoms to build Cu doped CoOOH slab, and a vacuum region of 20 Å above it was used to ensure the decoupling between neighboring systems. The geometry optimizations were performed until the forces on each ion was reduced below 0.01 eV/Å. The $3 \times 3 \times 1$ k-point sampling of the Brillouin zone was employed, and the DFT-D3 method were used to describe the van der Waals interaction [32].

The adsorption energy E_{ads} is calculated using the expression:

$$E_{ads} = E_{molecule+surface} - E_{surface} - E_{molecule}$$

where $E_{surface}$ is the energy of CoOOH slab or Cu doped CoOOH slab,

$E_{molecule}$ represents the energy of C₇H₈O. $E_{molecule+surface}$ represents the total energy of the adsorbed systems.

2.7. Quantitative analysis of the products

The products of BAOR were identified by gas chromatography (GC, GC-3400, Tianpu Instrument Co. Ltd., China). The concentration of the products was determined by the internal standard method and ethylbenzene was used as an internal standard substance. The measurement conditions of GC, and standard curves of the components were shown in Table S1 and Fig. S1. After the BAOR, the products were extracted from the electrolyte by ethyl acetate, as the following procedure: 500.0 μL electrolyte was removed from the anode under vigorous stirring per two hours, and then 500.0 μL HCl (1.0 mol·L⁻¹) was added to precipitate the benzoic acid. Subsequently, 1.0 mL ethyl acetate was dripped into the

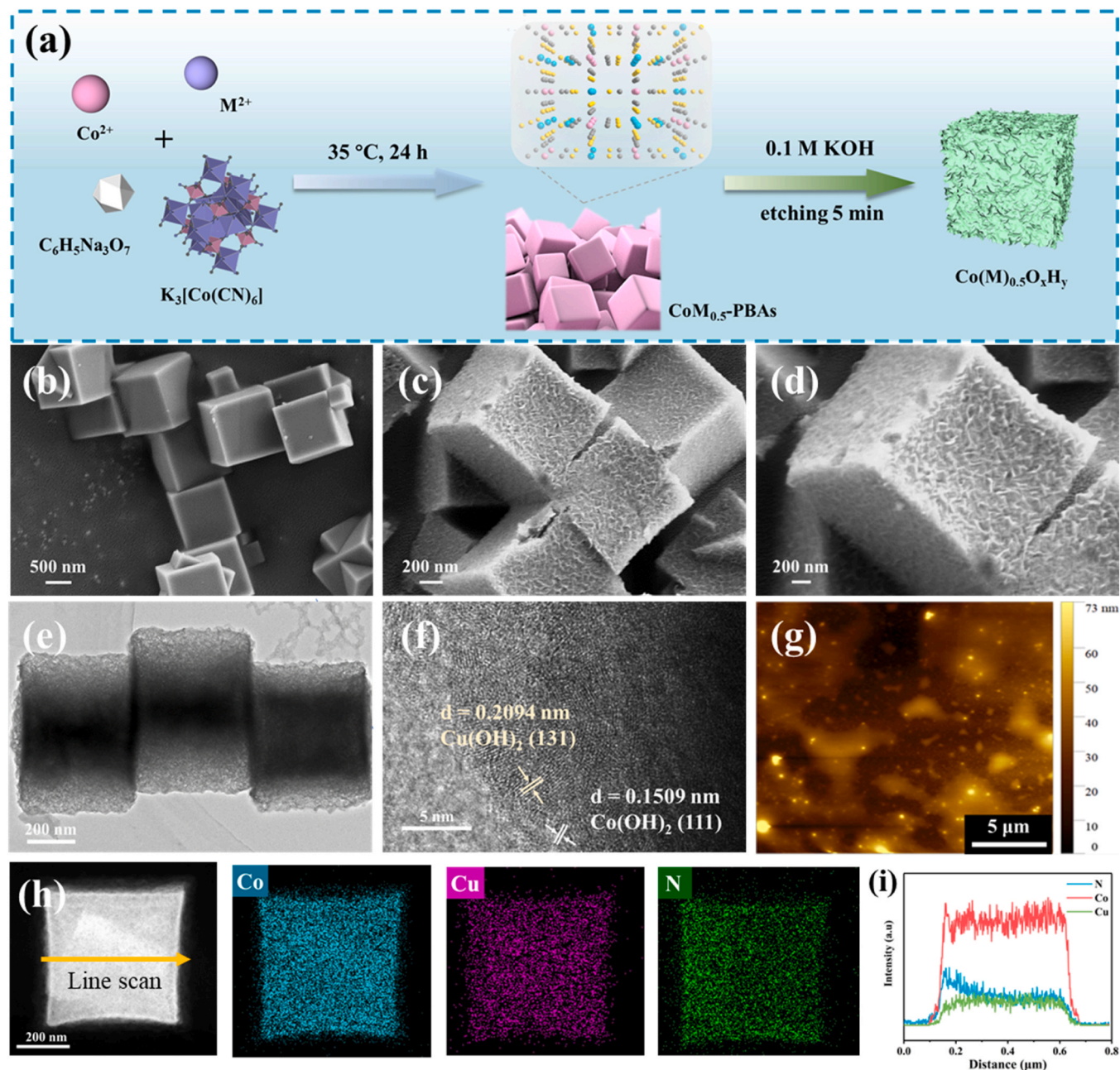


Fig. 1. (a) Schematic diagram of the manufacturing process of Co(M)_{0.5}O_xH_y; SEM images of (b) CoCu_{0.5}-PBAs, (c-d) Co(Cu)_{0.5}O_xH_y; (e) TEM image, (f) HR-TEM image, (g) AFM image, (h) EDX-mapping images, (i) Line scan analysis of Co(Cu)_{0.5}O_xH_y.

solution to extract benzoic acid. After sufficient oscillation, 200.0 μL supernatant solution was mixed with 200.0 μL ethylbenzene ($10.0 \text{ mmol}\cdot\text{L}^{-1}$).

The conversion rate, selectivity, benzoic acid yield, and Faraday efficiency (FE) were calculated by equations:

$$\text{Conversion } (\%) = \frac{n_0 - n}{n_0} \times 100\%$$

$$\text{Selectivity } (\%) = \frac{n_{\text{benzoic acid}}}{n_{\text{consumed benzyl alcohol}}} \times 100\%$$

$$\text{Yield}_{\text{total}} (\%) = \frac{n_{\text{products}}}{n_0} \times 100\%$$

$$\text{FE } (\%) = \frac{4 \times n_{\text{benzoic acid}} \times F}{Q} \times 100\%$$

Where n_0 and n represent for the molar quantity of benzyl alcohol before and after reaction, respectively. F is the Faraday constant ($96485 \text{ C}\cdot\text{mol}^{-1}$), and Q is the total electric charge.

3. Results and discussion

3.1. Insights of microstructure and composition of $\text{Co}(\text{M})_{0.5}\text{O}_x\text{H}_y$ ($\text{M} = \text{Cu, Ni, Mn, Zn}$)

The manufacturing process of bimetallic hydroxides $\text{Co}(\text{M})_{0.5}\text{O}_x\text{H}_y$ is illustrated in Fig. 1a. The $\text{CoM}_{0.5}$ -PBAs with micro-cubic structure (Fig. S2) was primarily synthesized and further served as the sacrificial templates in the subsequent process. After alkali etching, $\text{Co}(\text{CN})_6^{3-}$ in the $\text{CoM}_{0.5}$ -PBAs unit cell was substituted by the OH^- , and eventually formed the $\text{Co}(\text{M})_{0.5}\text{O}_x\text{H}_y$. The $\text{Co}(\text{M})_{0.5}\text{O}_x\text{H}_y$ ($\text{M} = \text{Cu, Co, Ni, Zn}$) exhibited micro-cubic profile, of which the surface was constructed by ultrafine lamellate arrays (Fig. 1b–e and Fig. S3). However, the cube of $\text{Co}(\text{Mn})_{0.5}\text{O}_x\text{H}_y$ were partially destroyed after reacting with KOH solution (Fig. S3b), which might be attributed to the cleavage of $\text{Mn}^{\text{II}}-\text{N}\equiv\text{C}-\text{Co}^{\text{III/II}}$ bond [33]. Such difference in morphology might cause the varying of catalytic activity. The high-resolution TEM (HR-TEM) images (Fig. 1f, Fig. S4) showed the poor crystal of $\text{Co}(\text{Cu})_{0.5}\text{O}_x\text{H}_y$, and the lattice fringes with spacing of 0.2094 nm and 0.1509 nm matched well with (131) facet of $\text{Cu}(\text{OH})_2$ and (111) facet of $\text{Co}(\text{OH})_2$, respectively. The surface roughness of $\text{Co}(\text{Cu})_{0.5}\text{O}_x\text{H}_y$ was approximately 8.20 nm (AFM images in Fig. 1g, Fig. S5), which was induced by the lamellate arrays. The uniform distribution of Co, Cu, and N elements over the microcubes in the selected region (Fig. 1h and i) was confirmed by the energy dispersive X-ray spectra mappings (EDX-mappings) and line scan analyses. Thereinto, the existence of N element is ascribed to the incomplete alkali etching.

The microcrystalline structure of $\text{CoM}_{0.5}$ -PBAs and $\text{Co}(\text{M})_{0.5}\text{O}_x\text{H}_y$ were further examined by XRD. As shown in Fig. S6, the extra-low content of M^{2+} , as well as its uniformly distribution status in the

microcubes, made the diffraction peaks of $\text{Co}(\text{M})_{0.5}$ -PBAs being in great accordance with Co-PBAs (PDF# 89–3737) [34]. After alkali etching, only broad diffraction peaks of $\text{Co}(\text{OH})_2$ (PDF# 74–1057) presented in the XRD patterns of $\text{Co}(\text{M})_{0.5}\text{O}_x\text{H}_y$ ($\text{M} = \text{Cu, Co, Ni, Zn}$), implying that $\text{M}(\text{OH})_2$ ($\text{M} = \text{Cu, Ni, Zn}$) might exist in partial amorphous texture (Fig. 2a) [9]. Nevertheless, three other diffraction peaks shown in the $\text{Co}(\text{Mn})_{0.5}\text{O}_x\text{H}_y$ were indexed to $\text{Mn}(\text{OH})_2$ (PDF# 44–1418), manifesting the more easily formation propensity of large hydroxide particle of $\text{Co}(\text{Mn})_{0.5}$ -PBAs [35]. The FTIR spectroscopy offered more detailed chemical composition of $\text{Co}(\text{Cu})_{0.5}\text{O}_x\text{H}_y$ (Fig. 2b). The intense peak at 2080 cm^{-1} was attributed to $\text{C}\equiv\text{N}$ vibration, further proving the insufficient alkali etching treatment [36]. In addition, the broad peaks at 628 cm^{-1} and 525 cm^{-1} were characteristic of Co–OH bending and Co–O stretching vibration in $\text{Co}(\text{OH})_2$, and 410 cm^{-1} peak was originated from Cu–OH stretching vibration in $\text{Cu}(\text{OH})_2$, illustrating that the $\text{Co}(\text{Cu})_{0.5}\text{O}_x\text{H}_y$ was composed of $\text{Co}(\text{OH})_2$ and $\text{Cu}(\text{OH})_2$ [9,37]. Moreover, the Raman spectra also revealed the existence of $\text{Co}(\text{OH})_2$ (520 cm^{-1} and 465 cm^{-1} peaks) in the $\text{Co}(\text{Cu})_{0.5}\text{O}_x\text{H}_y$ (Fig. 2c) [9,38]. There was no significant peaks of $\text{Cu}(\text{OH})_2$, which is due to the low content of Cu element.

The chemical state and molecular structure of elements in the electrocatalysts were further clarified by XPS spectra. The survey spectra of $\text{Co}(\text{M})_{0.5}\text{O}_x\text{H}_y$ clearly showed the presence of M (Cu, Mn, Zn, Ni), Co, O, and N elements in the catalysts (Fig. S7a–e). The peak position of Cu^{2+} (934.38 eV and 954.35 eV , Auger peak located at 568.0 eV) well matched the Cu 2p spectra of $\text{Cu}(\text{OH})_2$ (Fig. 3a and Fig. S7) [39,40]. The fitting peaks of Mn were corresponding to Mn^{3+} (643.68 eV and 655.01 eV) and Mn^{2+} (642.08 eV and 653.49 eV), which represented for Mn_2O_3 and $\text{Mn}(\text{OH})_2$, respectively (Fig. 3b) [14]. As for $\text{Co}(\text{Ni})_{0.5}\text{O}_x\text{H}_y$, the formation of $\text{Ni}(\text{OH})_2$ was confirmed by the Ni $2p_{3/2}$ (856.02 eV) and Ni $2p_{1/2}$ (873.50 eV) peaks [1]. The two symmetrical spin-orbit peaks at 1021.60 eV (Zn $2p_{3/2}$) and 1044.61 eV (Zn $2p_{1/2}$) reflected the formation of $\text{Zn}(\text{OH})_2$ in the $\text{Co}(\text{Zn})_{0.5}\text{O}_x\text{H}_y$ (Fig. 3d) [14]. These results proved the successfully synthesis of bimetallic hydroxides $\text{Co}(\text{M})_{0.5}\text{O}_x\text{H}_y$. The O 1s spectra demonstrated various oxygen species in the $\text{Co}(\text{M})_{0.5}\text{O}_x\text{H}_y$ (Fig. S8). The lattice OH species (531.06 eV) were observed in all spectra, which was indicative of a hydroxide ($\text{M}(\text{OH})_2$) structure in the near-surface [41]. A shift of lattice OH species could be clearly found in $\text{Co}(\text{M})_{0.5}\text{O}_x\text{H}_y$ ($\text{M} = \text{Mn, Ni, Zn}$), implying the decrease of electron density around OH^- species [14].

Introduction of M (Cu, Mn, Ni, and Zn) species into crystal was thought to be able to modulate the electronic structure of CoO_xH_y , thus the Co 2p spectra were analyzed. The peaks of Co^{2+} ($\approx 797.55 \text{ eV}$ and 782.38 eV) and Co^{3+} ($\approx 796.28 \text{ eV}$ and 780.76 eV) were detected in all specimens (Fig. 3e) [9], which was assigned to $\text{Co}(\text{OH})_2$ and $\text{Co}(\text{CN})_6^{3-}$, respectively. The increase of electron density in the Co nucleus was reflected by the peaks of Co 2p in $\text{Co}(\text{Cu})_{0.5}\text{O}_x\text{H}_y$ shifted toward the lower binding energies [14]. Besides, the minimum ratios of $\text{Co}^{3+}/\text{Co}^{2+} + \text{Co}^{3+}$ of $\text{Co}(\text{Mn})_{0.5}\text{O}_x\text{H}_y$ illustrated low content of $\text{Co}(\text{CN})_6^{3-}$ in the structure, which was considered to be the reason for the collapse of $\text{Co}(\text{Mn})_{0.5}\text{O}_x\text{H}_y$

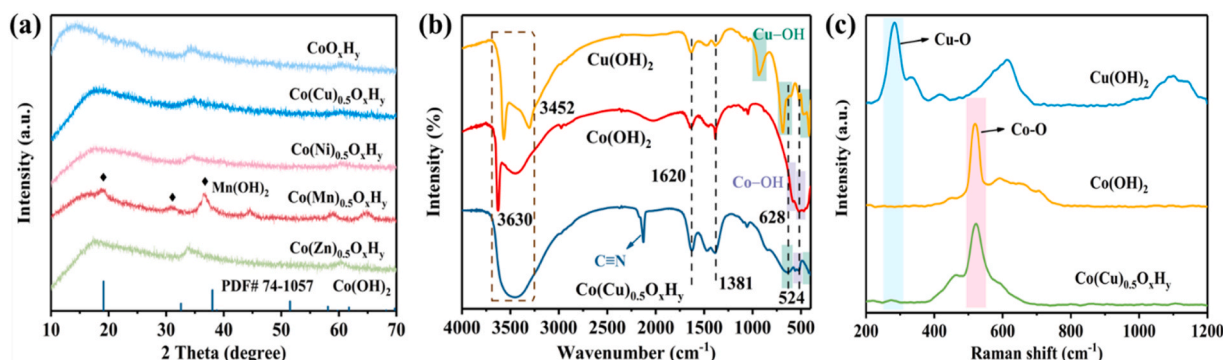


Fig. 2. (a) XRD patterns of as-prepared $\text{Co}(\text{M})_{0.5}\text{O}_x\text{H}_y$, (b) FTIR spectroscopy, (c) Raman spectroscopy of $\text{Co}(\text{Cu})_{0.5}\text{O}_x\text{H}_y$.

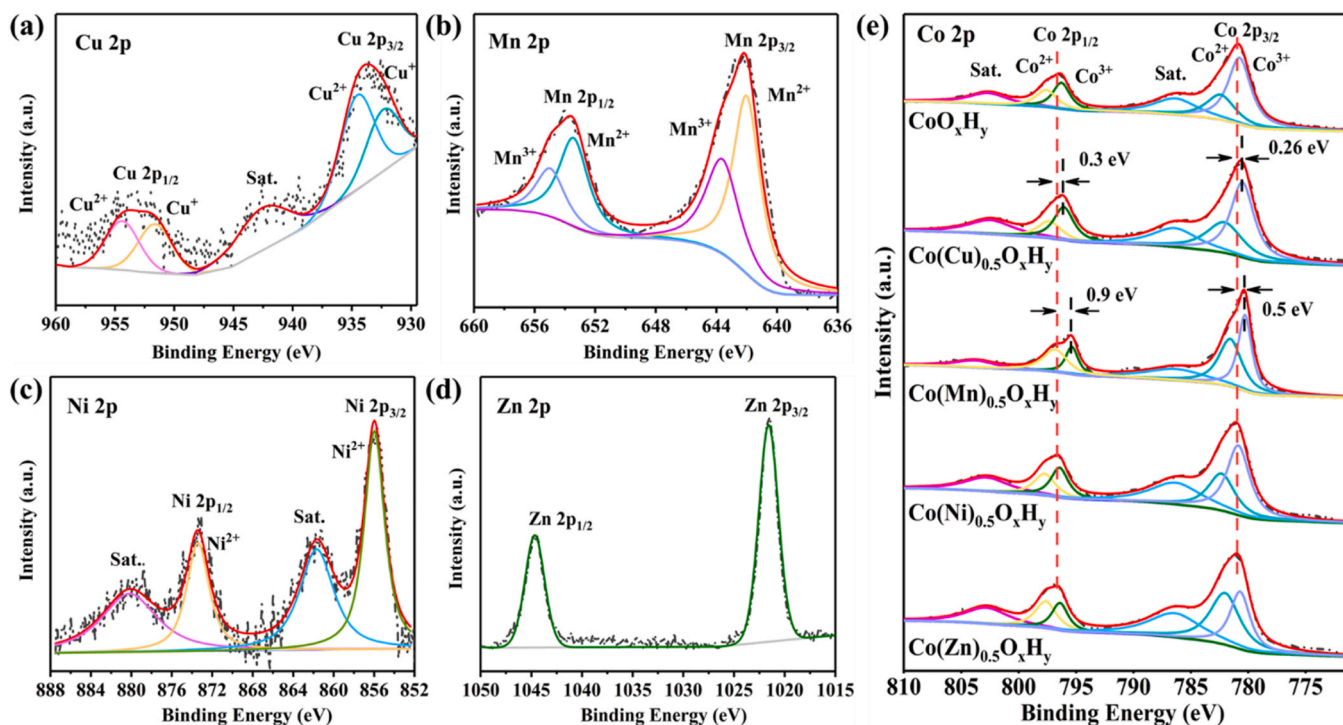


Fig. 3. XPS spectra of (a) Cu 2p, (b) Mn 2p, (c) Ni 2p, (d) Zn 2p, (e) Co 2p.

skeleton (Table S2).

3.2. Screening of electrocatalysts for BAOR

The OER performance was investigated firstly in 1.0 M KOH electrolyte, as shown in Fig. S9. The $\text{Co}(\text{Cu})_{0.5}\text{O}_x\text{H}_y$ catalyst exhibited superior OER performance. Its overpotential of 302.4 mV at $10 \text{ mA}\cdot\text{cm}^{-2}$ overwhelmed most of the other electrocatalysts for alkaline OER. It should be noted that, with the exception for $\text{Co}(\text{Mn})_{0.5}\text{O}_x\text{H}_y$, the overpotentials of other catalysts (Cu, Ni, Zn, Co) were relatively close, implying the lamellate arrays were vital for OER. BAOR was carried out in an H-type cell, as depicted in Fig. 4a. The polarization curves of $\text{Co}(\text{Cu})_{0.5}\text{O}_x\text{H}_y$ presented a larger current density than that of $\text{Co}(\text{Mn})_{0.5}\text{O}_x\text{H}_y$ (Co, Zn, Ni, Mn) in the potential range of 1.3 V – 1.6 V, revealing its excellent catalytic activity in the BAOR system (Fig. 4b). Additionally, the overpotential of $\text{Co}(\text{Cu})_{0.5}\text{O}_x\text{H}_y$ at $10 \text{ mA}\cdot\text{cm}^{-2}$ was 164.4 mV, which was 144 mV, 147 mV, and 156 mV lower than that of $\text{Co}(\text{Ni})_{0.5}\text{O}_x\text{H}_y$ (308.4 mV), $\text{Co}(\text{Zn})_{0.5}\text{O}_x\text{H}_y$ (311.4 mV) and CoO_xH_y (320.4 mV), respectively (Fig. S9). This might prove the fact that doping of Cu element could modulate the electronic density of Co active site, and eventually increase the adsorption energy of benzyl alcohol. Compared to the OER, the LSV curves of BAOR of $\text{Co}(\text{Cu})_{0.5}\text{O}_x\text{H}_y$ showed a positive trend at 1.30 V to 1.53 V, resulting in 138 mV reduction in the overpotential at $10 \text{ mA}\cdot\text{cm}^{-2}$. Such phenomenon could be ascribed to the interaction between catalyst and benzyl alcohol, which apparently accelerated the electron transfer. The benzyl alcohol conversion rate and the benzoic acid selectivity of $\text{Co}(\text{Cu})_{0.5}\text{O}_x\text{H}_y$ catalyst recorded at 0.5 V vs. Hg/HgO for 7 h electrolysis achieved 95.3% and 98.2%, respectively (Fig. 4c and Fig. S10), which were the best electrocatalysts among Co (Mn) $_{0.5}\text{O}_x\text{H}_y$. The contribution of the Ni foam was considered be quite limited to catalytic activity, namely the conversion rate of benzyl alcohol and the selectivity of benzoic acid was only 53.7% and 43.9%. The Faradic efficiency of $\text{Co}(\text{Cu})_{0.5}\text{O}_x\text{H}_y$ was 82.0%, which was lower than the other Co(Mn) $_{0.5}\text{O}_x\text{H}_y$ ($\text{M} = \text{Co}, \text{Ni}, \text{Zn}, \text{Mn}$) catalysts, indicating that the competing reaction OER might consume most of the electrons at 0.5 V vs. Hg/HgO (Fig. 4d). The formation rate of benzoic acid of $\text{Co}(\text{Cu})_{0.5}\text{O}_x\text{H}_y$ could reach up to $11.13 \text{ mmol}\cdot\text{g}^{-1}\cdot\text{h}^{-1}$, which was 1.85,

1.56, 1.68, and 1.63 times higher than $\text{Co}(\text{Mn})_{0.5}\text{O}_x\text{H}_y$ ($6.02 \text{ mmol}\cdot\text{g}^{-1}\cdot\text{h}^{-1}$), $\text{Co}(\text{Ni})_{0.5}\text{O}_x\text{H}_y$ ($7.13 \text{ mmol}\cdot\text{g}^{-1}\cdot\text{h}^{-1}$), $\text{Co}(\text{Zn})_{0.5}\text{O}_x\text{H}_y$ ($6.62 \text{ mmol}\cdot\text{g}^{-1}\cdot\text{h}^{-1}$) and CoO_xH_y ($6.82 \text{ mmol}\cdot\text{g}^{-1}\cdot\text{h}^{-1}$), respectively (Fig. 4e).

The change of benzyl alcohol concentration and benzoic acid total yield for $\text{Co}(\text{Cu})_{0.5}\text{O}_x\text{H}_y$ versus reaction time were displayed in Fig. 4f. As the reaction conducted, the reaction rate of benzyl alcohol decreased gradually and achieved the maximum conversion of 95.3%, the highest selectivity of 98.2%, as well as the total yield of 95.1% at the reaction proceeded for 7 h. Nevertheless, the Faradic efficiency dropped from 82.0% to 55.5%, which might be ascribed to the OER occurred in the system by reducing in benzyl alcohol concentration (Fig. 4g). Thus, it can be concluded that doping of Cu elements to regulate the electronic density of Co active sites was an effective method to promote the catalytic performance. The tandem oxidation of benzyl alcohol with water based on the $\text{Co}(\text{Cu})_{0.5}\text{O}_x\text{H}_y$ electrocatalyst possessed both superior conversion and selectivity, outperforming the other catalysts reported in the literature (Fig. 4h) [1,2,11,42–47].

The CdI was investigated to specify the active sites of $\text{Co}(\text{Cu})_{0.5}\text{O}_x\text{H}_y$, as displayed in Fig. S11 and S12. The CdI of $\text{Co}(\text{Cu})_{0.5}\text{O}_x\text{H}_y$ for both OER ($109.6 \text{ mF}\cdot\text{cm}^{-2}$) and BAOR ($118.5 \text{ mF}\cdot\text{cm}^{-2}$) were larger than that of Co (Mn) $_{0.5}\text{O}_x\text{H}_y$ ($\text{M} = \text{Co}, \text{Zn}, \text{Ni}, \text{Mn}$) catalysts, verifying the $\text{Co}(\text{Cu})_{0.5}\text{O}_x\text{H}_y$ possessing more active sites. Operando EIS was employed to reveal the interface behavior during the OER and BAOR (Fig. 5, Fig. S13–S17). Two equivalent circuit models were used to simulate the OER or BAOR reaction process of Co(Mn) $_{0.5}\text{O}_x\text{H}_y$ electrocatalysts at 1.33 V based on the Nyquist and Bode plots (Fig. S13). Only the high frequency interface existed charge transfer at 1.33 V for both OER and BAOR of Co (Mn) $_{0.5}\text{O}_x\text{H}_y$ ($\text{M} = \text{Co}, \text{Mn}, \text{Zn}$). Since, there was only electrocatalyst oxidation reaction occurred in the OER and BAOR system at 1.33 V considering the LSV curves. Thus, the catalyst electrooxidation reaction was proceeded at the high frequency interface (Fig. 5a and b, Fig. S15). Nevertheless, both high and low frequency interfaces existed charge transfer in the Co(Mn) $_{0.5}\text{O}_x\text{H}_y$ ($\text{M} = \text{Cu}$ and Ni), manifesting the BAOR and catalyst electrooxidation reaction happened at low frequency and high frequency interface, respectively. The fitted impedance parameters were displayed in Table S3. The $\text{Co}(\text{Cu})_{0.5}\text{O}_x\text{H}_y$ and $\text{Co}(\text{Ni})_{0.5}\text{O}_x\text{H}_y$ had

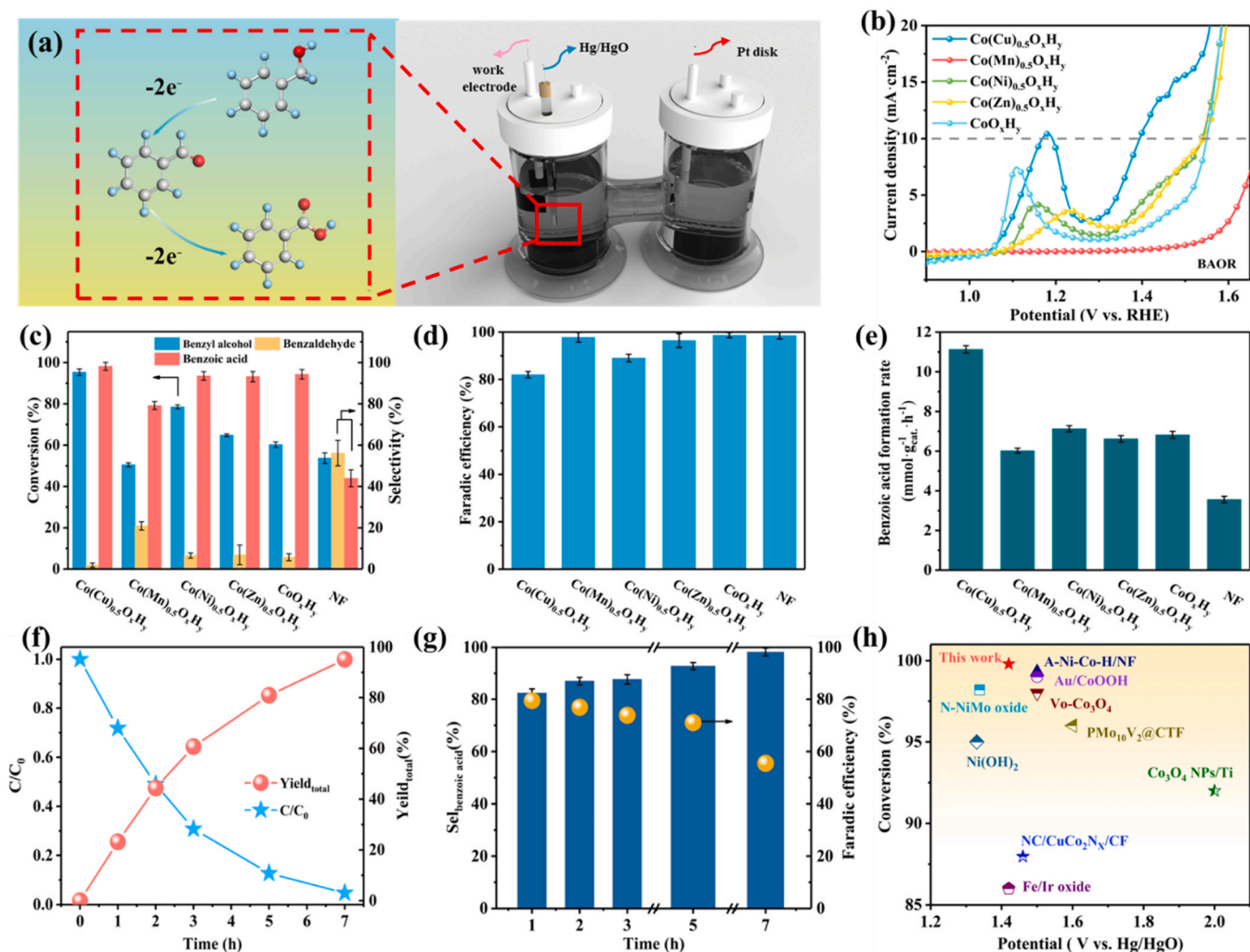


Fig. 4. (a) The schematic diagram of electrolytic cell and reaction process for electrocatalytic benzyl alcohol oxidation, (b) BAOR polarization curves of electrocatalysts, (c) BAOR performance of $\text{Co(M)}_{0.5}\text{O}_x\text{H}_y$ and NF under 0.5 V vs. Hg/HgO, (d) The Faradic efficiency of $\text{Co(M)}_{0.5}\text{O}_x\text{H}_y$ and NF under 0.5 V vs. Hg/HgO, (e) The formation rate of benzoic acid of electrocatalysts and NF, (f) The change of benzyl alcohol concentration and total yield of benzoic acid under the different reaction time, (g) The selectivity of benzoic acid and the conversion of benzyl alcohol during the reaction time, (h) Comparison of catalytic performance between this work and other electrocatalysts reported before.

smaller charge transfer resistance (R_{ct}) values than those of CoO_xH_y , $\text{Co(Mn)}_{0.5}\text{O}_x\text{H}_y$, and $\text{Co(Zn)}_{0.5}\text{O}_x\text{H}_y$, namely, introducing Cu and Ni would facilitate the catalyst electrooxidation rate and catalytic activity. To further reveal the interface behavior of $\text{Co(Cu)}_{0.5}\text{O}_x\text{H}_y$ in both OER and BAOR, EIS was measured under varying potentials (Fig. 5c and d, Fig. S16 and S17). The equivalent circuit models were shown in Fig. S14 and the fitted parameters were listed in Table S4. The extremely faint charge transfer at high frequency interface of OER at 1.03 to 1.08 V reflected the formation of a diffuse double layer (DDL) between $\text{Co(Cu)}_{0.5}\text{O}_x\text{H}_y$ and electrolyte [16]. The catalyst electrooxidation reaction took place at high frequency interface during OER at 1.13 to 1.43 V. Over 1.43 V, another semi-circle presented at low frequency interface with the occurrence of OER, further proving that OER occurred at low frequency interface (Fig. 5d and Fig. S16b). On the contrary, there was no significant charge transfer found at high frequency interface in BAOR system at 1.03 to 1.08 V, owing to the high frequency interface being in the DDL (Fig. 5d and Fig. S16a) [48]. A significant charge transfer phenomenon appeared in high frequency interface at 1.13 to 1.28 V during BAOR. This was indicative of the occurrence of $\text{Co(Cu)}_{0.5}\text{O}_x\text{H}_y$ electrooxidation reaction at high frequency interface (Fig. 5d and Fig. S16). Over 1.28 V, the current density increased obviously in the LSV curves, and a semi-circle emerged in low frequency interface of the

Bode plot. It was ascribed to the BAOR happened at low frequency interface (Fig. 5d and Fig. S16b). For both BAOR and OER system, the charge transfer resistance (R_{ct1}) at high frequency interface decreased with the increase of potential, because the electrooxidation rate of $\text{Co(Cu)}_{0.5}\text{O}_x\text{H}_y$ was accelerated (Table S4). The R_{ct2} at low frequency interface appeared during BAOR over 1.28 V. The R_{ct2} value of 1.53 V was larger than 1.43 V, illustrating that the mass transfer rate of OH^- was slower than that of BA molecule.

3.3. Mechanism analysis of BAOR for $\text{Co(Cu)}_{0.5}\text{O}_x\text{H}_y$

The structural evolution of $\text{Co(Cu)}_{0.5}\text{O}_x\text{H}_y$ during OER and BAOR was characterized by in-situ Raman spectroscopy (Fig. 6a and b, Fig. S18). The appearance of overlapping peak between 500 to 600 cm^{-1} after CV activation in 1 M KOH indicated a progressive oxidation of $\text{Co(Cu)}_{0.5}\text{O}_x\text{H}_y$ to $\text{Co(Cu)}_{0.5}\text{OOH}$ (Fig. S18) [49]. However, the Raman band at 687 cm^{-1} was assigned to CoO_6 octahedra of spinel Co_3O_4 [9]. This evaluation manifested the formation of Co_3O_4 after CV activation. Subsequently, the Raman spectra of OER under various anodic potentials were compared (Fig. 6a). No distinct variation of Raman peaks was observed at the resting state (OCP and 0.1 V vs. Hg/HgO), due to the equilibrium of electrode. Slight structural change can be observed at

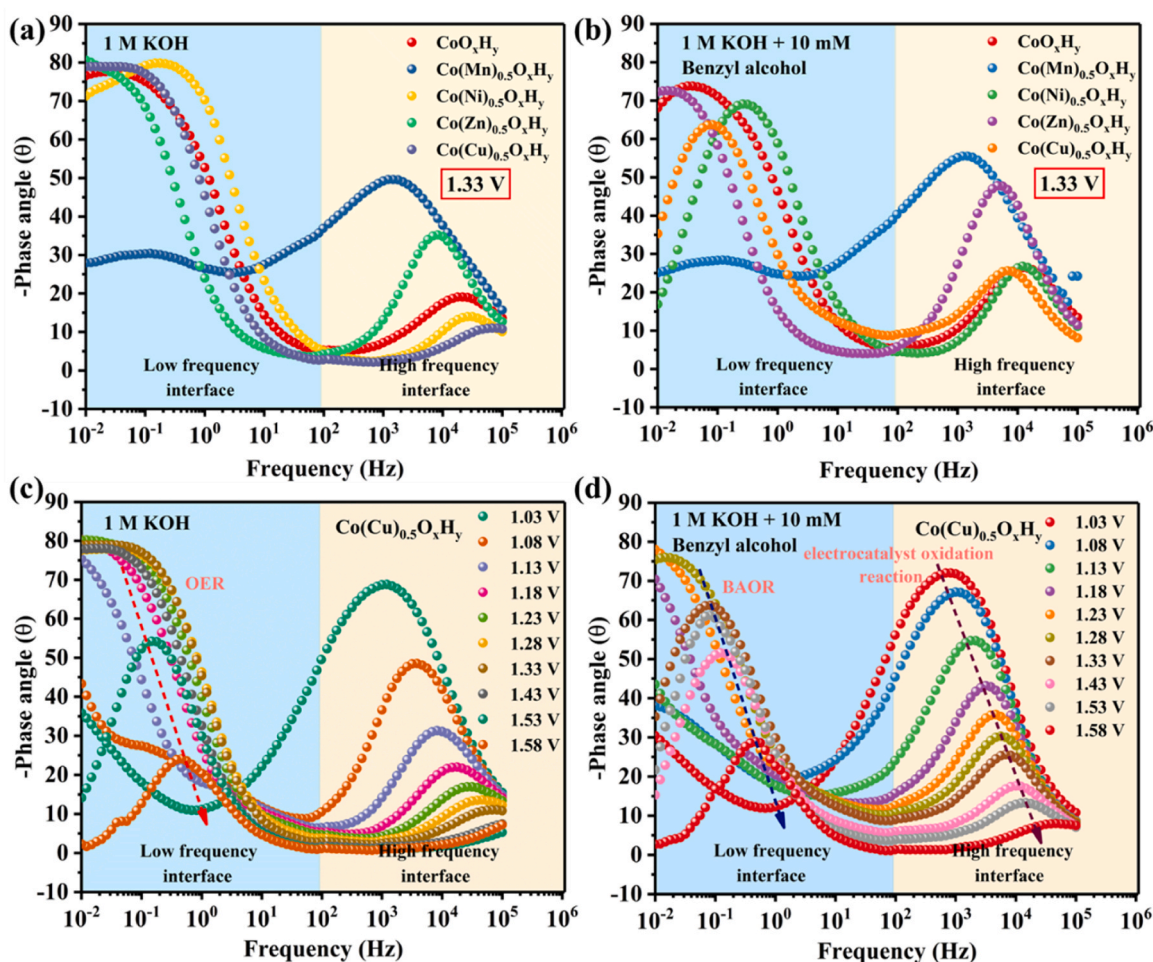


Fig. 5. Bode plots of as-prepared catalysts (a) 1 M KOH (b) 1 M KOH with 10 mM BA. Bode plots of $\text{Co}(\text{Cu})_{0.5}\text{O}_x\text{H}_y$ for (c) BAOR and (d) OER under different potentials.

0.2 V vs. Hg/HgO, where a subtle shoulder peak at 552 cm^{-1} (A_{1g}) arose. Such conversion was more pronounced at 0.3 V and 0.4 V vs. Hg/HgO, namely the band intensity of A_{1g} was strengthened and E_g (485 cm^{-1}) modes were shifted to low frequencies. Simultaneously, the peak intensity at 687 cm^{-1} attenuated. These features of Raman peaks were reminiscent of hexagonal LiCoO_2 , where the E_g band was attributed to the in-plane bending vibration of O–Co–O along a-b axis, and the A_{1g} band was ascribed to the stretching vibration of Co–O along c axis [50]. Nevertheless, a significant red shift of A_{1g} band (552 cm^{-1}) was observed compared to the phonon modes of LiCoO_2 (583 cm^{-1}) in the literature [50]. This ascribed to the insertion of Cu^{2+} into the CoO_2 slabs, leading to the enlargement of the c-axis [9,51]. Based on above results, the formation of amorphous CoOOH at an anodic potential of 0.2–0.4 V vs. Hg/HgO can be proposed ($\text{Co}(\text{OH})_2 + \text{OH}^- - e^- = \text{CoOOH} + \text{H}_2\text{O}$). As the anodic polarization raising to 0.5–0.6 V vs. Hg/HgO, the substantial configurational transformation was observed. The Raman active band at 687 cm^{-1} was nearly vanished, as well as the E_g band was slightly redshifted (472 cm^{-1}). This Raman band shift was similar to that of LiCoO_2 delithiation. The Raman modes of LiCoO_2 at 486 cm^{-1} will redshift to 475 cm^{-1} , when it underwent electrochemical oxidation [52]. Thus, the intermediates obtained by oxidation at 0.5–0.6 V vs. Hg/HgO was CoO_2 , as demonstrated by the well accordance with the Raman band positions ($\text{CoOOH} + \text{OH}^- - e^- = \text{CoO}_2 + \text{H}_2\text{O}$). Unlike the activation in OER system, the catalyst exhibited amorphous structure after activation in 1 M KOH with 10 mM BA (Fig. S18). Remarkable structural evolution was observed between 0.3–0.5 V vs. Hg/HgO (Fig. 6b). The transformation of $\text{Co}(\text{Cu})_{0.5}\text{O}_x\text{H}_y$ to $\text{Co}(\text{Cu})_{0.5}\text{OOH}$ was supported on the

basis of the presence of Raman band at 485 cm^{-1} and 552 cm^{-1} . The Raman mode at 620 cm^{-1} was attributed to amorphous CoO_x according to Chen et al. [53]. When the applied potential at 0.6 V vs. Hg/HgO, the characteristic bands resembled that of CoO_2 .

Considering the results of Raman and LSV, the real active site of BAOR was proposed. The progressive evolution of CoOOH to CoO_2 was hindered at 0.5 V vs. Hg/HgO in BAOR system. Meanwhile, the current density remarkably boosted. Probably, the correlation between BA molecules and CoO_2 was attributed to the instantaneous PCET process ($\text{Ph-CH}_2\text{OH} + \text{CoO}_2 = \text{CoOOH} + \text{Ph-CH}_2\text{O}^*$) [15]. The amperometric i-t curve at open circuit potential (OCP) proved the presence of instantaneous PCET process (Fig. 6c). After injecting 35.0 mmol BA into the electrolyte, the current density promptly raised to $2.25\text{ mA}\cdot\text{cm}^{-2}$. Such phenomenon confirmed that CoO_2 was the activity phase of BAOR. The evidence was also found in CV curves of BAOR and OER (Fig. 6d). The cathodic peak of Co^{4+} to Co^{3+} (0.5 V vs. Hg/HgO) disappeared after the addition of BA [54]. This feature illustrated the existence of PCET process between BA and Co^{4+} . Thus, the prediction of CoO_2 as the active origin of BAOR is well accordance with the periodic electrochemical measurements. Similar phenomenon was observed in $\text{Co}(\text{Ni})_{0.5}\text{O}_x\text{H}_y$ catalyst, but it was absent on the CoO_xH_y , $\text{Co}(\text{Zn})_{0.5}\text{O}_x\text{H}_y$, and $\text{Co}(\text{Mn})_{0.5}\text{O}_x\text{H}_y$. (Fig. S19). Briefly, Cu incorporation into the CoO_xH_y generated the structure more susceptible to transformation (Fig. S20).

Based on the in-situ Raman spectroscopy, the BAOR mechanism was further highlighted and two considerable evolutions in catalyst structure were insighted. $\text{Co}(\text{Cu})_{0.5}\text{OOH}$ was primarily formed by electro-oxidation in the high frequency at 0.2 V vs. Hg/HgO (Fig. 6e).

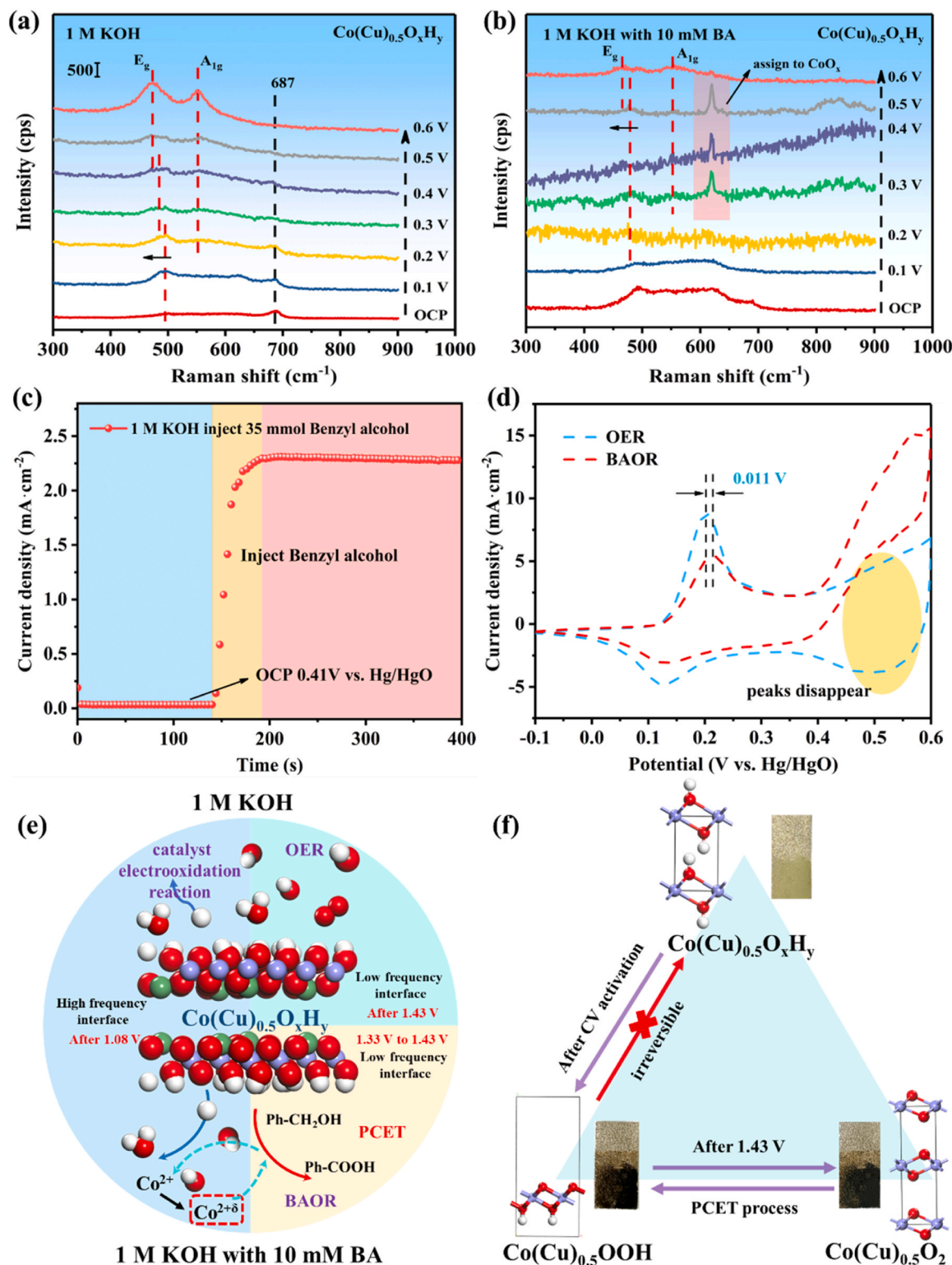


Fig. 6. In situ Raman spectra of $\text{Co(Cu)}_{0.5}\text{O}_x\text{H}_y$ in (a) 1 M KOH and (b) 1 M KOH with 10.0 mM BA, (c) i-t curve of BA injection at OCP, (d) CV curves of $\text{Co(Cu)}_{0.5}\text{O}_x\text{H}_y$ in 1.0 M KOH and 1.0 M KOH with 10.0 mM BA, Schematic diagram of (e) interface reaction occurring on catalyst, (f) the change of the valence state of Co during the BAOR.

Meanwhile, the color of electrocatalyst changed from yellow-green to black (Fig. 6d). When the anodic potential increased to 0.5 V vs. Hg/HgO, the $\text{Co(Cu)}_{0.5}\text{OOH}$ was progressively oxidized to dark olive green $\text{Co(Cu)}_{0.5}\text{O}_2$. Subsequently, the high valence Co^{4+} species robbed electrons and protons from the BA molecules, as described in the PCET process. Ultimately, the Co^{4+} was reduced to Co^{3+} , and BA was oxidized

to benzoic acid. This feature indicated the transformation from $\text{Co(Cu)}_{0.5}\text{OOH}$ to $\text{Co(Cu)}_{0.5}\text{O}_2$ was reversible. However, an irreversible conversion of $\text{Co(Cu)}_{0.5}\text{OOH}$ to $\text{Co(Cu)}_{0.5}\text{O}_x\text{H}_y$ was also observed using CV curves. This might be ascribed to the initial spinel structure of such catalyst [55]. With the potential raising to 0.6 V vs. Hg/HgO, the OER prior to BAOR was observed at low frequency interface. The

electrooxidation rate of Co^{3+} ($\text{Co}^{3+} - \text{e}^- = \text{Co}^{4+}$) was faster than that of PCET process, leading to the phase of catalyst transition to CoO_2 .

3.4. Confirmation of phase transition of $\text{Co}(\text{Cu})_{0.5}\text{O}_x\text{H}_y$ after BAOR

The structural evolution of the $\text{Co}(\text{Cu})_{0.5}\text{O}_x\text{H}_y$ catalyst after BAOR were also verified by combining XRD, TEM, FTIR, Raman, and XPS analyses. Two typical peaks at 19.2° and 34.8° representing Co-PBAs were eliminated after BAOR (Fig. 7a). The phase of catalyst could be proved transferring from $\text{Co}(\text{Cu})_{0.5}\text{O}_x\text{H}_y$ to $\text{Co}(\text{Cu})_{0.5}\text{OOH}$ by the diffraction peaks of CoOOH (PDF#: 07-0169) [9]. The results were well agreement with the in-situ Raman analysis (Fig. 6a and b), and it could thus be concluded the irreversible transformation of $\text{Co}(\text{Cu})_{0.5}\text{OOH}$ to $\text{Co}(\text{Cu})_{0.5}\text{O}_x\text{H}_y$. Additionally, the characteristic peak of $\text{Co}(\text{Cu})_{0.5}\text{OOH}$ located at 37.2° slightly shifted to low angle. This was attributed to the increase of interlayer spacing caused by the Cu atom doping [50]. Benefiting from the stable structure of MOFs, the micro-cubic morphology of catalyst was still clearly maintained after BAOR (Fig. 7b). The lattice fringe with spacing of 0.2429 nm was corresponding to (101) facet of CoOOH (Fig. 7c). Evidence of phase transition could also be reflected in FTIR spectra (Fig. 7d), that is, a sharp peak of the $\text{Co}(\text{Cu})_{0.5}\text{O}_x\text{H}_y$ catalyst after BAOR presented at 584 cm^{-1} was from the Co-O vibration in octahedral holes [56]. Besides, the structural transition during BAOR could be further identified by the existence of Co-O double bond (1651 cm^{-1}) [9] and the absence of $\text{C}\equiv\text{N}$ bond (2127 cm^{-1}) [36] in $\text{Co}(\text{Cu})_{0.5}\text{OOH}$. The structural details of $\text{Co}(\text{Cu})_{0.5}\text{O}_x\text{H}_y$ after BAOR was further monitored by Raman spectra, as depicted in Fig. S21. The formation of $\text{Co}(\text{Cu})_{0.5}\text{OOH}$ was proved by the representative phonon modes at 459.2 cm^{-1} , 504.1 cm^{-1} , 602.8 cm^{-1} , and 662.6 cm^{-1} [52]. The chemical states of Cu and Co on the catalyst surface after BAOR was investigated by XPS spectra (Fig. 7e). The binding energy of $\text{Co } 2p_{3/2}$ in $\text{Co}(\text{Cu})_{0.5}\text{OOH}$ was slightly shifted to lower energy ($\sim 0.4\text{ eV}$) than that of pristine $\text{Co}(\text{Cu})_{0.5}\text{O}_x\text{H}_y$, indicating the increase of electron density of Co [14]. Alternatively, the $\text{Cu } 2p_{3/2}$ for $\text{Co}(\text{Cu})_{0.5}\text{OOH}$ (Fig. 7f) exhibited positive shift ($\sim 0.5\text{ eV}$), because of the

charge transfer from Cu to Co.

3.5. Understanding the synergies between Cu and Co elements

The function of Cu species doping in electrocatalyst was illustrated by DFT calculations. A mono-layer 4×4 CoOOH slab and $\text{Co}(\text{Cu})_{0.5}\text{OOH}$ slab were constructed, as displayed in Fig. S22. The catalytic reaction was initiated the adsorption of the reactant on the active sites of the catalyst. Therefore, calculating the adsorption energy of the reactants on the catalyst surface is a vital criterion to judge the reaction performance. In consideration of the parallel adsorption has a strong chemical stability and more energetically reasonable [57], BA molecule was placed on the CoOOH and $\text{Co}(\text{Cu})_{0.5}\text{OOH}$ slab in parallel, denoting as CoOOH-ADS and $\text{Co}(\text{Cu})_{0.5}\text{COOH-ADS}$, respectively (Fig. S23). The corresponding energy of CoOOH slab, $\text{Co}(\text{Cu})_{0.5}\text{COOH}$ slab, CoOOH-ADS , $\text{Co}(\text{Cu})_{0.5}\text{COOH-ADS}$, and BA molecule were listed in Table S5. The adsorption energies (E_{ads}) of BA on CoOOH and $\text{Co}(\text{Cu})_{0.5}\text{COOH}$ slab were demonstrated in Fig. 8a. Because the BA was more easily enriched on the $\text{Co}(\text{Cu})_{0.5}\text{OOH}$ catalyst surface, the E_{ads} of BA on $\text{Co}(\text{Cu})_{0.5}\text{OOH}$ slab (-3.922 eV) was remarkably larger than that on CoOOH (-0.841 eV). This is why the reduction peak of Co^{4+} to Co^{3+} in $\text{Co}(\text{Cu})_{0.5}\text{O}_x\text{H}_y$ disappeared in CV curve (Fig. 6d and Fig. S19). The DOS at the Fermi level (E_F) was 0, it might declared the semiconductor properties of CoOOH (Fig. 8b) [58]. However, after introducing Cu species, the $\text{Co}(\text{Cu})_{0.5}\text{OOH}$ exhibited metallic properties with a new DOS appearing near the E_F (Fig. 8c). The partial density of states (PDOS) was further analyzed to clarify the strong interactions between BA and slab. The PDOS of Co 3d orbitals in CoOOH and O 2p orbitals in BA molecule were highly coincident near the Fermi level, demonstrating that the BA molecule was adsorbed on CoOOH surface by d-p coupling (Fig. 8d) [12]. However, the PDOS of Co 3d orbitals for $\text{Co}(\text{Cu})_{0.5}\text{OOH}$ crossed the Fermi level (Fig. 8e), illustrating that the electrons were transferred from Cu to Co [27]. This increase in electron density of Co induced the enhancement of the adsorption energy of BA. The conclusion is pivotal as it elucidated the decrease of the R_{ct} for $\text{Co}(\text{Cu})_{0.5}\text{O}_x\text{H}_y$ during BAOR.

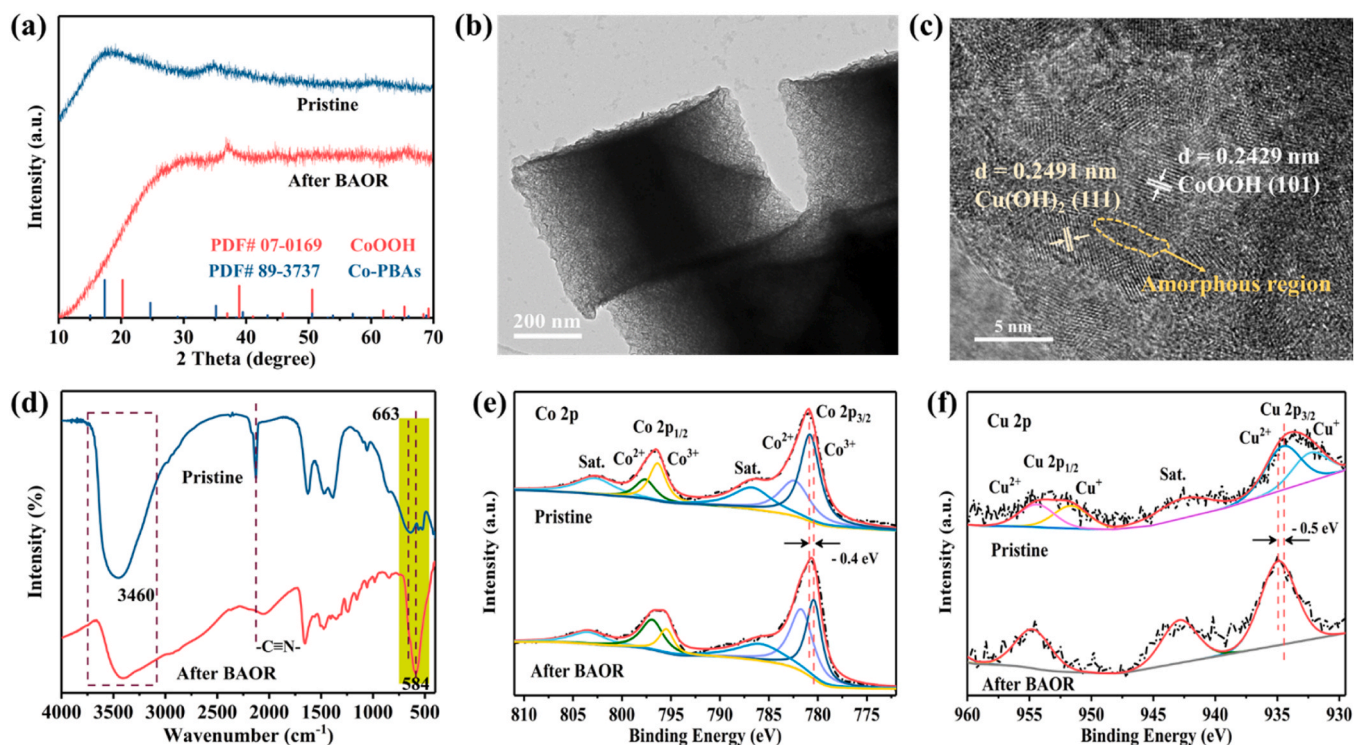


Fig. 7. (a) XRD patterns of $\text{Co}(\text{Cu})_{0.5}\text{O}_x\text{H}_y$ and $\text{Co}(\text{Cu})_{0.5}\text{OOH}$, (b, c) TEM and HRTEM images of $\text{Co}(\text{Cu})_{0.5}\text{OOH}$, (d) FTIR of $\text{Co}(\text{Cu})_{0.5}\text{O}_x\text{H}_y$ and $\text{Co}(\text{Cu})_{0.5}\text{OOH}$, XPS spectra of $\text{Co}(\text{Cu})_{0.5}\text{O}_x\text{H}_y$ and $\text{Co}(\text{Cu})_{0.5}\text{OOH}$ (e) Co 2p, and (f) Cu 2p.

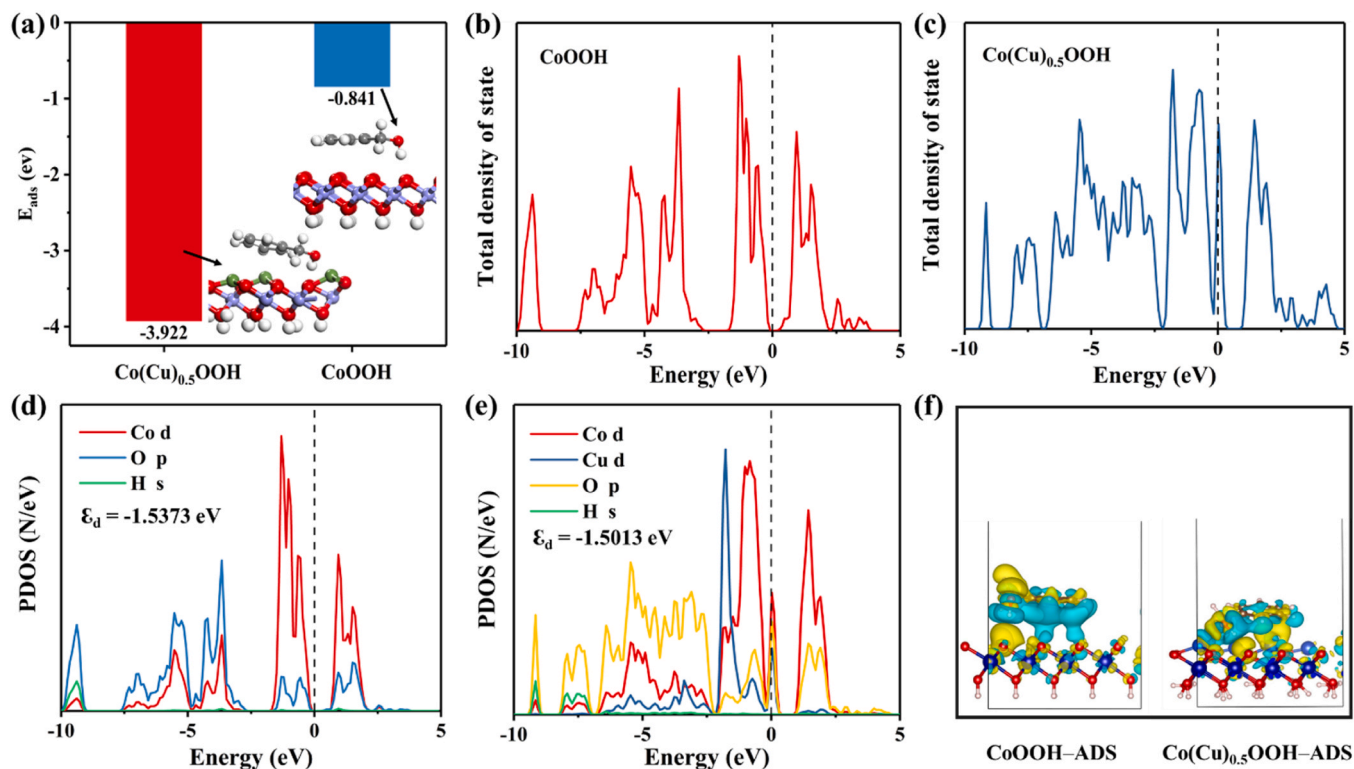


Fig. 8. (a) Adsorption energies of BA on the Co(Cu)_{0.5}OOH and CoOOH, Total DOS of (b) CoOOH and (c) Co(Cu)_{0.5}OOH, (d) PDOS of Co 3d, O 2p, and H 1 s; (e) PDOS of Co 3d, Cu 3d, O 2p, and H 1 s; (f) The difference charge densities of CoOOH (left) and Co(Cu)_{0.5}OOH (right).

Additionally, the shift of E_F towards the valence band (Fig. 8c) indicated that the introduction of Cu species belonged to p-type doping. This p-type semiconductors could provide abundant electron holes with oxidation activity [59]. These evidences forcefully supported the synergistic effect of Cu doping in promoting the BAOR activity of CoO_xH_y. The Cu 3d orbitals crossing the E_F was attributed to hybridization between the Co 3d and Cu 3d orbitals [27]. The shift of d-band center to Fermi level after Cu doping (-1.5013 eV) was from the improvement of the adsorption capacity of BA. This was in great accordance with the calculated results of adsorption energies. The discrepancy charge density of CoOOH-ADS slab and Co(Cu)_{0.5}OOH-ADS slab were investigated, as illustrated in Fig. 8f. The blue area and yellow area represented charge loss and charge accumulation, respectively. For CoOOH-ADS (left), the BA molecule lost charge, and the surface O of the CoOOH gained charge. Conversely, the charge transferred from the Cu atom to BA molecule after Cu doping, which was well agreement with the XPS analysis (Fig. 7e and f). Briefly, from the DFT simulation results, the incorporation of Cu atom in CoO_xH_y could enhance the adsorption capacity of BA molecule and consequently improve the BAOR performance.

3.6. Optimization on reaction process

To obtain the best catalytic performance, the key factors influencing the BAOR, including molar ratio of Cu and Co, electrolytic potential and BA concentration were optimized. The Cu content in catalyst determined by ICP-OES was listed in Table S6. The BAOR was carried out under 0.5 V vs. Hg/HgO for 7 h. The FE and yield of benzoic acid as a function of Cu doping amount was demonstrated in Fig. 9a. The yield of benzoic acid dramatically rose from 52.09% to 93.85%, while the FE decreased from 94.95% to 82.00% with the Cu doping increased from 0.1 to 0.5. Alternatively, continuously increasing the Cu content to 0.9 led to negligible changes in FE and benzoic acid yield. The conversion rate of BA reached the maximum of 95.3% at Cu content of 0.5 (Fig. 9b).

The selectivity of benzoic acid and benzaldehyde principally maintain at 99.0% and 1.0% after doping Cu over 0.1. Possibly, the excessive doping of Cu atom had less impact on the conversion rate of BA. The electrolytic potential was the driving force of the electrocatalytic reaction and its magnitude would affect the reaction rate and product distribution. As shown in Fig. 9c and Fig. S24a–e, the conversion of BA obviously enhanced from 61.3% to 95.3% with the electrolysis potential rising from 0.4 V to 0.5 V vs. Hg/HgO. It tended to be constant with further increasing the potential. From LSV curves (Fig. S25), we conjectured that the minimal change in conversion rate was attributed to the occurrence of OER in the system. The selectivity of benzaldehyde decreased with the potential increasing. This might be ascribed to the slower desorption rate on the catalyst surface induced by the lower solubility of the generated benzaldehyde in aqueous solution. Normally, the charge transfer will be accelerated with the potential rising. Consequently, the benzaldehyde will be further oxidized to benzoic acid, when the charge transfer was greater than the desorption rate of benzaldehyde. It is well consistency with the EIS analysis (Fig. S16). The formation rate of benzoic acid could attain to $13.5 \text{ mmol} \cdot \text{g}_{\text{cat}}^{-1} \cdot \text{h}^{-1}$ at 0.6 V vs. Hg/HgO (Fig. 9d). However, the FE correspondingly dropped from 97.6% (at 0.4 V vs. Hg/HgO) to 47.6% (at 0.6 V vs. Hg/HgO) (Fig. S24f), implying the formation of oxygen. The CoCu_{0.5}O_xH_y catalyst could achieve a maximum formation rate of benzoic acid ($29.8 \text{ mmol} \cdot \text{g}_{\text{cat}}^{-1} \cdot \text{h}^{-1}$) at the concentration of $60 \text{ mmol} \cdot \text{L}^{-1}$ (Fig. 9e). Nevertheless, the slow mass transfer induced by the high concentration resulted in the poor FE and lower BA conversion rate (Fig. S26). The relatively outstanding catalytic reaction conditions were thus determined as: molar ratio of Cu to Co 0.5:1, the electrolytic potential 0.5 V vs. Hg/HgO, and BA concentration $20 \text{ mmol} \cdot \text{L}^{-1}$.

The stability of the CoCu_{0.5}O_xH_y catalyst was evaluated under the optimal reaction conditions. The selectivity of benzoic acid and the conversion of BA continuously maintained at 97% and 80% within 6 cycles, representing excellent stability of the CoCu_{0.5}O_xH_y catalyst (Fig. 9f). Furthermore, no obvious attenuation of FE (over 80%) was

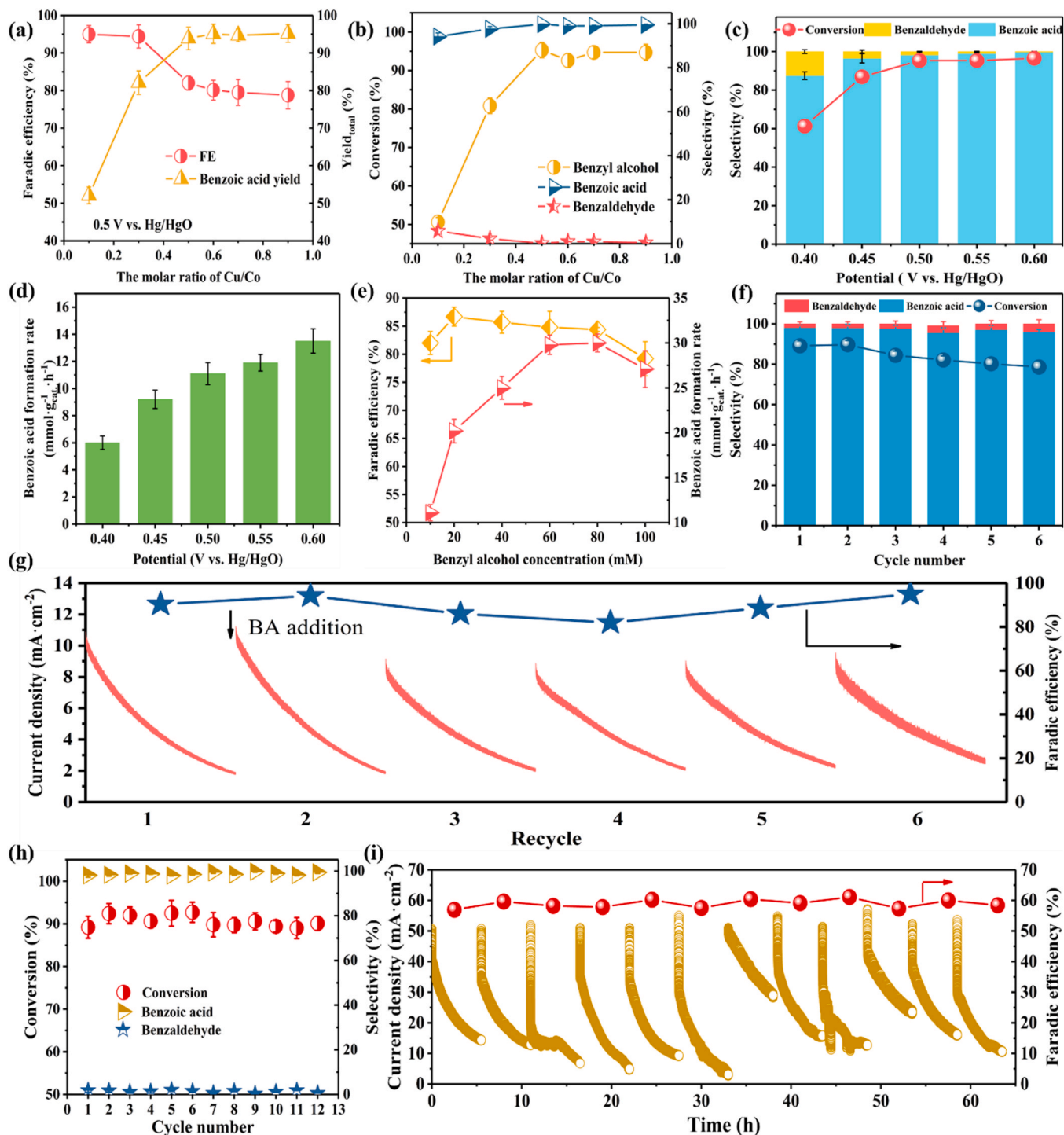


Fig. 9. (a) The FE and total yield of benzoic acid vs. the molar ratio of Cu/Co, (b) the conversion rate of BA and the selectivity of product vs. the molar ratio of Cu/Co, (c) the conversion of BA and the selectivity of product vs. electrolysis potential, (d) the formation rate of benzoic acid, (e) the FE and formation rate of benzoic acid at various concentration of BA, (f) Catalytic performance within 6 cycles at 10 mA·cm⁻², (g) FE and current density in recycling at 10 mA·cm⁻², (h) Catalytic performance within 12 cycles at 50 mA·cm⁻², (i) FE and current density in cycle at 50 mA·cm⁻².

found, as described in Fig. 9g. Roughly, the rapid current density decreasing in each cycle was attributed to the continuous consumption of BA. To further confirm the stability of the Co(Cu)_{0.5}O_xH_y at high current density, the durability test was performed at 50 mA·cm⁻² for 60 h (12 cycles). The Co(Cu)_{0.5}O_xH_y catalyst still exhibited outstanding conversion rate of benzyl alcohol (90%) and selectivity of benzoic acid (99.5%) after 12 cycles (Fig. 9h). However, the 60% of the FE is mainly attributed to the occurrence of OER at high current (Fig. 9i). The purity

of products separated after 6 cycles were further analyzed by nuclear magnetic resonance (NMR). Benzoic acid peaks were detected solely in ¹H spectrum and ¹³C spectrum, reflecting its excellent purity, as depicted in Fig. S27.

4. Conclusion

Utilizing the flexible structure of PBAs, a series of Co(M)_{0.5}O_xH_y (M

= Cu, Zn, Mn, Ni) catalysts were fabricated via a facile alkali etching strategy. It was found that $\text{Co}(\text{Cu})_{0.5}\text{O}_{x}\text{H}_y$ catalyst exhibited remarkable electrooxidation activity of BA with a $11.13 \text{ mmol} \cdot \text{g}_{\text{cat}}^{-1} \cdot \text{h}^{-1}$ formation rate of benzoic acid under 1.43 V. After the optimization the reaction parameters, the formation rate of benzoic acid was promoted to $20.2 \text{ mmol} \cdot \text{g}_{\text{cat}}^{-1} \cdot \text{h}^{-1}$ and the conversion rate of BA remained at 85.0%. Through analyzing the valence states of Co element and surface substances of the $\text{Co}(\text{Cu})_{0.5}\text{O}_{x}\text{H}_y$ during BAOR, the mechanism that BAOR was a spontaneous PCET process between Co^{4+} species and BA molecule ($\text{Ph}-\text{CH}_2\text{OH} + \text{CoO}_2 + \text{e}^- = \text{CoOOH} + \text{Ph}-\text{CH}_2\text{O}^-$) was proposed. Therefore, Co^{4+} species was the real active site of BAOR. DFT calculation revealed that such outstanding performance was attributed to the d-d orbital hybridized of Cu and Co causing the d orbital of Co shifted to Fermi level, thus enhancing the adsorption energy of BA molecule. Moreover, electrons of Cu atom were transferred to Co atom, creating abundant electron holes with strong oxidation activity in the catalyst. This study confirmed that the active site of Co-based catalyst in the BAOR process was Co^{4+} , and d-d orbital hybridized could significantly promote the catalytic activity. It is expected that this work could shed light on the design of Co-based catalysts.

CRedit authorship contribution statement

Zhang Jun: Data curation. **Huang Lei:** Conceptualization, Data curation, Formal analysis. **Zhang Ke:** Formal analysis. **Wang Yong-gang:** Supervision. **Wang Caihong:** Formal analysis. **Qu Sijian:** Supervision. **Lin Xiongchao:** Funding acquisition, Methodology, Project administration, Supervision, Writing – review & editing.

Declaration of Competing Interest

The authors declare that they have no known competing financial interests or personal relationships that could have appeared to influence the work reported in this paper.

Data Availability

The authors do not have permission to share data.

Acknowledgements

This work was supported by the National Natural Science Foundation of China [Grant numbers 22278420, 21978319, 22008253]; Central Universities outstanding youth team project of CUMTB (2023YQTD03).

Appendix A. Supporting information

Supplementary data associated with this article can be found in the online version at [doi:10.1016/j.apcatb.2024.123739](https://doi.org/10.1016/j.apcatb.2024.123739).

References

- L. Ming, X.-Y. Wu, S.-S. Wang, W. Wu, C.-Z. Lu, Facile growth of transition metal hydroxide nanosheets on porous nickel foam for efficient electrooxidation of benzyl alcohol, *Green. Chem.* 23 (2021) 7825–7830.
- J. Wan, X. Mu, Y. Jin, J. Zhu, Y. Xiong, T. Li, R. Li, Nitrogen-doped nickel-molybdenum oxide as a highly efficient electrocatalyst for benzyl alcohol oxidation, *Green. Chem.* 24 (2022) 4870–4876.
- D. Feng, Y. Dong, L. Zhang, X. Ge, W. Zhang, S. Dai, Z.-A. Qiao, Holey lamellar high-entropy oxide as an ultra-high-activity heterogeneous catalyst for solvent-free aerobic oxidation of benzyl alcohol, *Angew. Chem. Int. Ed. Engl.* 59 (2020) 19503–19509.
- X. Wu, Y. Wang, Z.-S. Wu, Design principle of electrocatalysts for the electrooxidation of organics, *Chem* 8 (2022) 2594–2629.
- Z. Wang, B. Zhang, S. Yang, X. Yang, F. Meng, L. Zhai, Z. Li, S. Zhao, G. Zhang, Y. Qin, Dual Pd^{2+} and Pd^0 sites on CeO_2 for benzyl alcohol selective oxidation, *J. Catal.* 414 (2022) 385–393.
- J. Pritchard, L. Kesavan, M. Piccinini, Q. He, R. Tiruvalam, N. Dimitratos, J. A. Lopez-Sanchez, A.F. Carley, J.K. Edwards, C.J. Kiely, G.J. Hutchings, Direct synthesis of hydrogen peroxide and benzyl alcohol oxidation using Au–Pd catalysts prepared by sol immobilization, *Langmuir* 26 (2010) 16568–16577.
- B. Mahmoudi, A. Rostami, M. Kazemnejadi, B.A. Hamah-Ameen, Catalytic oxidation of alcohols and alkyl benzenes to carbonyls using $\text{Fe}_3\text{O}_4/\text{SiO}_2$ @(TEMPO)-co-(Chlorophyll-CoIII) as a bi-functional, self-co-oxidant nanocatalyst, *Green. Chem.* 22 (2020) 6600–6613.
- G. Szczepaniak, J. Piatkowski, W. Nogas, F. Lorandi, S.S. Yerneni, M. Fantin, A. Ruszczynska, A.E. Enciso, E. Bulska, K. Grela, K. Matyjaszewski, An isocyanide ligand for the rapid quenching and efficient removal of copper residues after Cu/TEMPO-catalyzed aerobic alcohol oxidation and atom transfer radical polymerization, *Chem. Sci.* 11 (2020) 4251–4262.
- P. Gao, Y. Zeng, P. Tang, Z. Wang, J. Yang, A. Hu, J. Liu, Understanding the synergistic effects and structural evolution of $\text{Co}(\text{OH})_2$ and Co_3O_4 toward boosting electrochemical charge storage, *Adv. Funct. Mater.* 32 (2021).
- B. Qiu, L. Cai, Y. Wang, X. Guo, S. Ma, Y. Zhu, Y.H. Tsang, Z. Zheng, R. Zheng, Y. Chai, Phosphorus incorporation into Co_9S_8 nanocages for highly efficient oxygen evolution catalysis, *Small* 15 (2019) e1904507.
- Y. Cao, D. Zhang, X. Kong, F. Zhang, X. Lei, Multi-vacancy Co_3O_4 on nickel foam synthesized via a one-step hydrothermal method for high-efficiency electrocatalytic benzyl alcohol oxidation, *J. Mater. Sci.* 56 (2021) 6689–6703.
- J. Chen, Y. Wang, M. Zhou, Y. Li, Boosting the electro-oxidation of 5-hydroxy-methyl-furfural on a Co- CoS_2 heterojunction by intensified spin polarization, *Chem. Sci.* 13 (2022) 4647–4653.
- A. Arjunan, M. Manikandan, R. Vijayaraghavan, P. Sangeetha, Highly active and recyclable $\text{Cu}_3\text{Fe}_{3-x}\text{O}_4$ NPs for selective oxidation of benzyl alcohol using TBHP as an oxidant, *ChemistrySelect* 8 (2023) e202202776.
- K. Zheng, J. Ren, X. Li, G. Li, L. Jiao, C. Xu, Engineering crystalline CoMP-decorated ($\text{M} = \text{Mn}, \text{Fe}, \text{Ni}, \text{Cu}, \text{Zn}$) amorphous CoM LDH for high-rate alkaline water splitting, *Chem. Eng. J.* 441 (2022).
- W. Chen, Y. Wang, B. Wu, J. Shi, Y. Li, L. Xu, C. Xie, W. Zhou, Y.C. Huang, T. Wang, S. Du, M. Song, D. Wang, C. Chen, J. Zheng, J. Liu, C.L. Dong, Y. Zou, J. Chen, S. Wang, Activated Ni-OH bonds in a catalyst facilitates the nucleophile oxidation reaction, *Adv. Mater.* 34 (2022) e2105320.
- W. Chen, C. Xie, Y. Wang, Y. Zou, C.-L. Dong, Y.-C. Huang, Z. Xiao, Z. Wei, S. Du, C. Chen, B. Zhou, J. Ma, S. Wang, Activity origins and design principles of nickel-based catalysts for nucleophile electrooxidation, *Chem* 6 (2020) 2974–2993.
- H. Zhou, Z. Li, S.-M. Xu, L. Lu, M. Xu, K. Ji, R. Ge, Y. Yan, L. Ma, X. Kong, L. Zheng, H. Duan, Selectively upgrading lignin derivatives to carboxylates through electrochemical oxidative C(OH)–C bond cleavage by a mn-doped cobalt oxyhydroxide catalyst, *Angew. Chem. Int. Ed. Engl.* 60 (2021) 8976–8982.
- A. Moysiadiou, S. Lee, C.-S. Hsu, H.M. Chen, X. Hu, Mechanism of oxygen evolution catalyzed by cobalt oxyhydroxide: cobalt superoxide species as a key intermediate and dioxygen release as a rate-determining Step, *J. Am. Chem. Soc.* 142 (2020) 11901–11914.
- W. Kang, R. Wei, H. Yin, D. Li, Z. Chen, Q. Huang, P. Zhang, H. Jing, X. Wang, C. Li, Unraveling sequential oxidation kinetics and determining roles of multi-cobalt active sites on Co_3O_4 catalyst for water oxidation, *J. Am. Chem. Soc.* 145 (2023) 3470–3477.
- Q. Wu, J. Liang, M. Xiao, C. Long, L. Li, Z. Zeng, A. Mavric, X. Zheng, J. Zhu, H. W. Liang, H. Liu, M. Valant, W. Wang, Z. Lv, J. Li, C. Cui, Non-covalent ligand-oxygen interaction promotes oxygen evolution, *Nat. Commun.* 14 (2023) 997.
- J.G. McAlpin, Y. Surendranath, M. Dincă, T.A. Stich, S.A. Stojan, W.H. Casey, D. G. Nocera, R.D. Britt, EPR evidence for $\text{Co}(\text{IV})$ species produced during water oxidation at neutral pH, *J. Am. Chem. Soc.* 132 (2010) 6882–6883.
- J.B. Gerken, J.G. McAlpin, J.Y.C. Chen, M.L. Rigsby, W.H. Casey, R.D. Britt, S. S. Stahl, Electrochemical water oxidation with cobalt-based electrocatalysts from pH 0–14: the thermodynamic basis for catalyst structure, stability, and activity, *J. Am. Chem. Soc.* 133 (2011) 14431–14442.
- L. Zhang, W. Cai, N. Bao, H. Yang, Implanting an electron donor to enlarge the d-p hybridization of high-entropy (Oxy)hydroxide: a novel design to boost oxygen evolution, *Adv. Mater.* 34 (2022) 2110511.
- L. Gao, X. Li, Z. Yao, H. Bai, Y. Lu, C. Ma, S. Lu, Z. Peng, J. Yang, A. Pan, H. Huang, Unconventional p-d hybridization interaction in PtGa ultrathin nanowires boosts oxygen reduction electrocatalysis, *J. Am. Chem. Soc.* 141 (2019) 18083–18090.
- Q.Q. Pang, Z.L. Niu, S.S. Yi, S. Zhang, Z.Y. Liu, X.Z. Yue, Hydrogen-etched bifunctional sulfur-defect-rich ReS_2/CC electrocatalyst for highly efficient HER and OER, *Small* 16 (2020) e2003007.
- R. Li, P. Ren, P. Yang, Y. Li, H. Zhang, A. Liu, S. Wen, J. Zhang, M. An, Bimetallic co-doping engineering over nickel-based oxy-hydroxide enables high-performance electrocatalytic oxygen evolution, *J. Colloid Interface Sci.* 631 (2023) 173–181.
- C. Chen, M. Sun, F. Zhang, H. Li, M. Sun, P. Fang, T. Song, W. Chen, J. Dong, B. Rosen, P. Chen, B. Huang, Y. Li, Adjacent Fe Site boosts electrocatalytic oxygen evolution at Co site in single-atom-catalyst through a dual-metal-site design, *Energy Environ. Sci.* 16 (2023) 1685–1696.
- L. Zhang, H.B. Wu, X.W. Lou, Metal-organic-frameworks-derived general formation of hollow structures with high complexity, *J. Am. Chem. Soc.* 135 (2013) 10664–10672.
- G. Kresse, J. Hafner, Ab initio molecular-dynamics simulation of the liquid-metal-amorphous-semiconductor transition in germanium, *Phys. Rev. B* 49 (1994) 14251–14269.
- G. Kresse, D. Joubert, From ultrasoft pseudopotentials to the projector augmented-wave method, *Phys. Rev. B* 59 (1999) 1758–1775.
- B. Hammer, L.B. Hansen, J.K. Nørskov, Improved adsorption energetics within density-functional theory using revised Perdew-Burke-Ernzerhof functionals, *Phys. Rev. B* 59 (1999) 7413–7421.

- [32] S. Grimme, J. Antony, S. Ehrlich, H. Krieg, A consistent and accurate ab initio parametrization of density functional dispersion correction (DFT-D) for the 94 elements H-Pu, *J. Chem. Phys.* 132 (2010) 154104.
- [33] X. Song, S. Song, D. Wang, H. Zhang, Prussian blue analogs and their derived nanomaterials for electrochemical energy storage and electrocatalysis, *Small Methods* 5 (2021) e2001000.
- [34] P. Jiang, J. Chen, C. Wang, K. Yang, S. Gong, S. Liu, Z. Lin, M. Li, G. Xia, Y. Yang, J. Su, Q. Chen, Tuning the activity of carbon for electrocatalytic hydrogen evolution via an iridium-cobalt alloy core encapsulated in nitrogen-doped carbon cages, *Adv. Mater.* 30 (2018) 1705324.
- [35] X. Song, A. Emin, Y. Chen, M. Yang, S. Zou, Y. Du, Y. Fu, Y. Li, Y. Li, J. Li, D. He, Mn(OH)₂-coated Ni₃S₂ nanosheets on Ni foam as a cathode for high-performance aqueous asymmetric supercapacitors, *J. Energy Storage* 51 (2022) 104513.
- [36] Y. Wang, J. Ma, J. Wang, S. Chen, H. Wang, J. Zhang, Interfacial scaffolding preparation of hierarchical PBA-based derivative electrocatalysts for efficient water splitting, *Adv. Energy Mater.* 9 (2019).
- [37] K. Okada, R. Ricco, Y. Tokudome, M.J. Styles, A.J. Hill, M. Takahashi, P. Falcaro, Copper conversion into Cu(OH)₂ nanotubes for positioning Cu₃(BTC)₂ MOF crystals: controlling the growth on flat plates, 3D architectures, and as patterns, *Adv. Funct. Mater.* 24 (2014) 1969–1977.
- [38] T. Yoon, K.S. Kim, One-step synthesis of CoS-doped β-Co(OH)₂@Amorphous MoS₂-x hybrid catalyst grown on nickel foam for high-performance electrochemical overall water splitting, *Adv. Funct. Mater.* 26 (2016) 7386–7393.
- [39] S. Anantharaj, H. Sugime, S. Noda, Ultrafast growth of a Cu(OH)₂-CuO nanoneedle array on Cu foil for methanol oxidation electrocatalysis, *ACS Appl. Mater. Interfaces* 12 (2020) 27327–27338.
- [40] Y. Wang, W. Zhou, R. Jia, Y. Yu, B. Zhang, Unveiling the activity origin of a copper-based electrocatalyst for selective nitrate reduction to ammonia, *Angew. Chem. Int. Ed. Engl.* 59 (2020) 5350–5354.
- [41] Z. Chen, L. Cai, X. Yang, C. Kronawitter, L. Guo, S. Shen, B.E. Koel, Reversible structural evolution of NiCoO_xH_y during the oxygen evolution reaction and identification of the catalytically active phase, *ACS Catal.* 8 (2018) 1238–1247.
- [42] Y. Huang, R. Yang, G. Anandhababu, J. Xie, J. Lv, X. Zhao, X. Wang, M. Wu, Q. Li, Y. Wang, Cobalt/Iron(Oxides) heterostructures for efficient oxygen evolution and benzyl alcohol oxidation reactions, *ACS Energy Lett.* 3 (2018) 1854–1860.
- [43] Z. Li, J. Zhang, X. Jing, J. Dong, H. Liu, H. Lv, Y. Chi, C. Hu, A polyoxometalate@covalent triazine framework as a robust electrocatalyst for selective benzyl alcohol oxidation coupled with hydrogen production, *J. Mater. Chem. A* 9 (2021) 6152–6159.
- [44] Z. Yin, Y. Zheng, H. Wang, J. Li, Q. Zhu, Y. Wang, N. Ma, G. Hu, B. He, A. Knop-Gericke, R. Schlögl, D. Ma, Engineering interface with one-dimensional Co₃O₄ nanostructure in catalytic membrane electrode: toward an advanced electrocatalyst for alcohol oxidation, *ACS Nano* 11 (2017) 12365–12377.
- [45] J. Zheng, X. Chen, X. Zhong, S. Li, T. Liu, G. Zhuang, X. Li, S. Deng, D. Mei, J.-G. Wang, Hierarchical porous NC@CuCo nitride nanosheet networks: highly efficient bifunctional electrocatalyst for overall water splitting and selective electrooxidation of benzyl alcohol, *Adv. Funct. Mater.* (27) (2017).
- [46] Z. Li, Y. Yan, S.M. Xu, H. Zhou, M. Xu, L. Ma, M. Shao, X. Kong, B. Wang, L. Zheng, H. Duan, Alcohols electrooxidation coupled with H₂ production at high current densities promoted by a cooperative catalyst, *Nat. Commun.* 13 (2022) 147.
- [47] H. Huang, C. Yu, X. Han, H. Huang, Q. Wei, W. Guo, Z. Wang, J. Qiu, Ni, Co hydroxide triggers electrocatalytic production of high-purity benzoic acid over 400 mA cm⁻², *Energy Environ. Sci.* 13 (2020) 4990–4999.
- [48] M.E.G. Lyons, M.P. Brandon, The significance of electrochemical impedance spectra recorded during active oxygen evolution for oxide covered Ni, Co and Fe electrodes in alkaline solution, *J. Electroanal. Chem.* 631 (2009) 62–70.
- [49] J. Ren, N. Jiang, K. Shang, N. Lu, J. Li, Y. Wu, Synergistic degradation of transferic acid by water falling film DBD plasma coupled with cobalt oxyhydroxide: performance and mechanisms, *Chem. Eng. J.* 372 (2019) 321–331.
- [50] Y. Li, G. Chen, Y. Zhu, Z. Hu, T.S. Chan, S. She, J. Dai, W. Zhou, Z. Shao, Activating both basal plane and edge sites of layered cobalt oxides for boosted water oxidation, *Adv. Funct. Mater.* 31 (2021).
- [51] H.X. Yang, Y. Xia, Y.G. Shi, H.F. Tian, R.J. Xiao, X. Liu, Y.L. Liu, J.Q. Li, Raman spectroscopy study of α-, β-, γ-Na_xCoO₂ and γ-(Ca,Sr)_xCoO₂, *Phys. Rev. B* 74 (2006) 094301.
- [52] B.S. Yeo, A.T. Bell, Enhanced activity of gold-supported cobalt oxide for the electrochemical evolution of oxygen, *J. Am. Chem. Soc.* 133 (2011) 5587–5593.
- [53] C.-W. Tung, Y.-Y. Hsu, Y.-P. Shen, Y. Zheng, T.-S. Chan, H.-S. Sheu, Y.-C. Cheng, H. M. Chen, Reversible adapting layer produces robust single-crystal electrocatalyst for oxygen evolution, *Nat. Commun.* 6 (2015) 8106.
- [54] L. Cao, F. Xu, Y.Y. Liang, H.L. Li, Preparation of the novel nanocomposite Co(OH)₂/ultra-stable Y zeolite and its application as a supercapacitor with high energy density, *Adv. Mater.* 16 (2004) 1853–1857.
- [55] L. Trotochaud, J.K. Ranney, K.N. Williams, S.W. Boettcher, Solution-cast metal oxide thin film electrocatalysts for oxygen evolution, *J. Am. Chem. Soc.* 134 (2012) 17253–17261.
- [56] A. Yavuz, P. Yilmaz Erdogan, N. Ozdemir, H. Zengin, G. Zengin, M. Bedir, Electrochemical synthesis of CoOOH-Co(OH)₂ composite electrode on graphite current collector for supercapacitor applications, *J. Mater. Sci. Mater. Electron* 30 (2019) 18413–18423.
- [57] M. Jin, Y. Liu, X. Zhang, J. Wang, S. Zhang, G. Wang, Y. Zhang, H. Yin, H. Zhang, H. Zhao, Selective electrocatalytic hydrogenation of nitrobenzene over copper-platinum alloying catalysts: experimental and theoretical studies, *Appl. Catal. B* 298 (2021).
- [58] L. Long, D. Cao, J. Fei, J. Wang, Y. Zhou, Z. Jiang, Z. Jiao, H. Shu, Effect of surface intrinsic defects on the structural stability and electronic properties of the all-inorganic halide perovskite CsPbI₃ (0 0 1) film, *Chem. Phys. Lett.* 734 (2019) 136719.
- [59] M. Choi, S. Yagi, Y. Ohta, K. Kido, T. Hayakawa, Estimation of delafossite p-type CuGaO₂/ZnO hybrids as semiconductor photocatalyst by controlling particle size, *J. Phys. Chem. Solids* 150 (2021) 109845.